Elastography: ultrasonic estimation and imaging of the elastic properties of tissues

J Ophir[1,2]*, **S K Alam**[1†], **B Garra**[3‡], **F Kallel**[1], **E Konofagou**[1,2], **T Krouskop**[4] and **T Varghese**[1]
[1] Department of Radiology, The University of Texas Medical School, Houston, Texas, USA
[2] Bioengineering Program, University of Houston, Texas, USA
[3] Department of Radiology, Georgetown University Medical Center, Washington, DC, USA
[4] Baylor College of Medicine, Houston, Texas, USA

Abstract: The basic principles of using sonographic techniques for imaging the elastic properties of tissues are described, with particular emphasis on elastography. After some preliminaries that describe some basic tissue stiffness measurements and some contrast transfer limitations of strain images are presented, four types of elastograms are described, which include axial strain, lateral strain, modulus and Poisson's ratio elastograms. The strain filter formalism and its utility in understanding the noise performance of the elastographic process is then given, as well as its use for various image improvements. After discussing some main classes of elastographic artefacts, the paper concludes with recent results of tissue elastography *in vitro* and *in vivo*.

Keywords: elastography, elastogram, elasticity, Young's modulus, stress, strain, ultrasound, imaging, elastic modulus, Poisson's ratio, breast, prostate, kidney

1 INTRODUCTION

Predicting and understanding the behaviour of materials when they are subject to mechanical forces is the basis for many aspects of modern engineering practice, from the design of structures to the design of solid propellant rockets [1]. In the early development of the field of mechanics, studying the behaviour of materials often involved applying loads to the system until the system failed, and then the failure mechanism was studied and used to infer the behaviour of the material prior to failure. Then, as technology advanced, it became possible to study the behaviour of complex material systems using non-destructive testing procedures, e.g. X-ray analysis, acoustic behaviour and photoelastic behaviour. The results of the experimental studies have contributed to the development of understanding how materials behave and to the development of mathematical models that help predict the behaviour of more complex material systems that are fashioned in very complex patterns [2].

In contrast to engineering materials, biological tissues are not very well behaved, in the sense of being easily

described in closed-form mathematical expressions, because they are time and moisture dependent. When living, they are metabolically active and exhibit certain mechanical properties, which change soon after death. Moreover, these mechanical properties may be age, strain rate and strain range dependent [3–6]. To simplify the characterization of a tissue when the loading is of short enough duration that the viscous nature of the material can be ignored, the tissue can be assumed to behave elastically. This means that the state of the tissue only depends on the current loading; there is no effect from previous loading. By idealizing the tissue as an elastic material, the task of describing its behaviour is reduced to a matrix of 81 stiffness constants that must be specified [1]. Since obtaining these constants is a very challenging process, additional assumptions are often made to reduce the complexity of describing the tissue behaviour [7].

It is important to recognize the assumptions that are often employed to create a simple mathematical model of a tissue system. Tissue has a hierarchical structure and by choosing the scale or size of the tissue samples that are being studied, it is often possible to assume that the tissue is orthotropic, so the number of constants is reduced to 27. Then, by further restricting the scale of the sample so that the small structures in the system are randomly and uniformly distributed in the sample, the assumption of homogeneity is usefully employed so that only 12 constants are needed to describe the tissue.

Again, if the scale of the tissue is picked with care, it may be appropriate to approximate the tissue as an isotropic material so that only two constants are needed to describe the tissue's response to mechanical loads. These two constants are the Lamé constants, or their technical derivatives, Young's modulus and Poisson's ratio.

The elastic properties of soft tissues depend on their molecular building blocks, and on the microscopic and macroscopic structural organization of these blocks [8]. The standard medical practice of the soft tissue palpation is based on qualitative assessment of the low-frequency stiffness of tissue. Pathological changes are generally known to be correlated with changes in tissue stiffness as well. Many cancers, such as scirrhous carcinoma of the breast, appear as extremely hard nodules [9]. In many cases, despite the difference in stiffness, the small size of a pathological lesion and/or its location deep in the body preclude its detection and evaluation by palpation. In general, the lesion may or may not possess echogenic properties which would make it ultrasonically detectable. For example, tumours of the prostate or the breast could be invisible or barely visible in standard ultrasound examinations, yet be much harder than the embedding tissue [10]. Diffuse diseases such as cirrhosis of the liver are known to significantly increase the stiffness of the liver tissue as a whole [9], yet they may appear normal in conventional ultrasound examination. Since the echogenicity and the stiffness of tissue are generally uncorrelated, it is expected that imaging tissue stiffness or strain will provide new information that is related to pathological tissue structure. This expectation has now been confirmed [10]. In addition to pathology, there is additional evidence that various *normal* tissue components possess consistent differences in their stiffness parameters as well. For example, in the ovine kidney, the stiffness contrast between the cortex and the medullary pyramids has recently been measured to be only about 6 dB, and strain images showing easily discernible contrast have been made [11]. This observation provides the basis for imaging the normal anatomy as well.

Over the past 20 years there have been numerous investigations conducted to characterize the mechanical properties of biological tissue systems [3–6, 12–21] which have been idealized often as homogeneous, isotropic elastic materials. Much of the work has focused on bone, dental materials and vascular tissue. There are articles that discuss methods used to characterize these tissues and there is a large volume of experimental data about the mechanical response of these tissues to various types of loadings [17, 22–27]; however, there is a void in the retrievable literature regarding the mechanical properties of tissue systems tested *in vivo*. In fact, there is very limited information about the mechanical properties of most of the soft tissue systems that make up the body's organs. Yamada's book [21] presents a relatively broad range of data, but much of the data are derived

from experiments using animal tissues and all of the information relates to uniaxial tensile tests of the tissue.

The stiffness parameter cannot be measured directly. A mechanical stimulus of some kind must be propagated into the tissue, and precision means for detecting the resulting internal tissue motions must be provided. Such means may include ultrasound, magnetic resonance imaging (MRI) or other diagnostic imaging modalities. In the last 15 years, interest has been mounting in the ultrasonic imaging of tissue elasticity parameters. A comprehensive literature review of this field can be found in Ophir *et al.* [25] and in Gao *et al.* [17], and will not be repeated here. Tissue elasticity imaging methods based on ultrasonics fall into two main groups: (a) methods where a quasi-static compression is applied to the tissue and the resulting components of the strain tensor are estimated [24, 28, 29] and (b) methods where a low-frequency vibration is applied to the tissue and the resulting tissue behaviour is inspected [23, 30–33]. Among the techniques based on the quasi-static estimation of tissue strain, elastography [24] is based on estimating the tissue strain using a correlation algorithm, whereas another elasticity imaging technique [28] is based on estimating such strain using signal phase information. Most importantly, however, in both methods, local tissue displacements are estimated from the time delays between gated pre- and post-compression echo signals, whose axial gradient is then computed to estimate and display the local strain. Recently, intravascular application of elastographic techniques have also been reported [34–36]. In this paper, emphasis is placed on describing the recent progress in elastography, which is being developed in the authors' laboratory. Among the second group of techniques, in sonoelasticity imaging [30, 31], the vibration amplitude pattern of the shear waves in the tissue under investigation is detected using Doppler methods, and a corresponding colour image (similar to a colour Doppler display) is superimposed on the conventional grey-scale image. An absence of vibration may signify the presence of tumours. A theory of sonoelasticity imaging was developed [37] and an *in vitro* study on excised human prostate showed better sensitivity and specificity than conventional transrectal ultrasound [38]. Yamakoshi *et al.* [32] developed a method to map both the amplitude and the phase of low-frequency wave propagation in the tissue. These can be used to derive the velocity and dispersion properties of the wave propagation. Krouskop *et al.* [23] used a single-element pulsed Doppler instrument to measure the tissue flow at points of interest under external vibration.

Somewhat later, a parallel development has occurred in MRI. Plewes *et al.* [39] have developed a method that is based on the compression of the tissue and estimation of the resultant strains using MRI. Fowlkes *et al.* [40] have discussed an MRI-based method to measure tissue displacements. They have also shown mathematical reconstruction of the distribution of the moduli for select

examples. Muthupillai *et al.* [41] developed an MRI method similar to the ultrasonic Doppler method described by Yamakoshi *et al.* [32].

First some basic tissue stiffness results are presented which demonstrate the existence of stiffness contrast among normal tissues and between normal and pathological tissues in the breast and prostate. These data provide the continued motivation for further development of this field. Then the elastographic process is described, starting from the tissue elastic modulus distribution, progressing through various algorithms for precision time delay estimation of echoes from strained tissues and culminating in the production of the elastogram. Several kinds of elastograms are then described, each displaying a different quantity, which is related to the elastic properties of the tissue, and each having been derived using different methodologies. These include axial strain, lateral strain, modulus and Poisson's ratio elastograms [42]. The use of ultrasound to acquire tissue motion information results in certain basic limitations on the attainable elastographic image parameters, which may be described by the theoretical framework known as the strain filter [43]. The strain filter may be used to predict and design important improvements to various elastographic image attributes, such as dynamic range expansion and improvement in the signal-to-noise ratio in elastography (SNRe) through multiresolution processing [44]. In combination with certain contrast transfer efficiencies (CTEs) inherent in the conversion of the modulus to strain contrast [45, 46], the strain filter formalism may be used to predict the upper bound as well as the practically attainable performance of the contrast-to-noise ratio in elastography (CNRe). After a brief description of the mechanical, acoustic and signal processing artefacts that may be encountered in the practice

of elastography, recent results that demonstrate that quality elastograms may be produced and interpreted under low and high elastic contrast conditions are produced for both *in vitro* and *in vivo* studies.

2 BASIC DATA ON TISSUE STIFFNESS

Very little basic data are available in the literature on the stiffness of soft tissues. Perhaps this is due to the fact that, until recently, such data were of no practical consequence. However, the paucity of data does not change the well-known fact that tissue elasticity is intimately related to the higher levels of tissue organization. In view of the present ability to visualize the elastic attributes of tissues, it is inevitable that more data will become available in the ensuing years. Some data have been collected by Sarvazyan *et al.* [47], Parker *et al.* [48] and Walz *et al.* [49]. Some of the authors' recent results on breast and prostate tissues *in vitro* are given in Table 1 [50]. These results indicate that in the normal breast fibrous tissues are stiffer than glandular tissues, which are in turn stiffer than adipose tissues. The two kinds of tumours studied show different behaviours, with the infiltrating ductal carcinomas being significantly stiffer than the ductal tumours. Some of the tissues exhibit marked non-linear changes in their stiffness behaviour with applied precompressive strain, while others remain unchanged. There appear to be opportunities in differentiating breast tissues based on their stiffness values as well as their non-linear stiffness behaviour. Significant differences are also evident among normal, BPH and cancerous tissues of the prostate (Table 2).

Table 1 Results of actual stiffness measurements (in kPa) of normal and abnormal breast tissues *in vitro*

Strain rate	5% pre-compression			20% pre-compression		
	1%/s	10%/s	40%/s	2%/s	20%/s	80%/s
Normal fat ($n = 40$)	18 ± 7	19 ± 7	22 ± 9	20 ± 8	20 ± 6	23 ± 5
Normal glandular ($n = 31$)	28 ± 14	33 ± 11	35 ± 14	48 ± 15	57 ± 19	66 ± 17
Fibrous ($n = 21$)	97 ± 33	107 ± 32	118 ± 83	220 ± 88	233 ± 59	245 ± 83
Ductal CA ($n = 23$)	22 ± 8	25 ± 4	26 ± 5	291 ± 67	301 ± 58	307 ± 78
Infiltrating ductal CA ($n = 32$)	106 ± 32	93 ± 33	112 ± 43	558 ± 180	490 ± 112	460 ± 178

Table 2 Results of actual stiffness measurements (in kPa) of normal and abnormal prostate tissues *in vitro* (BPH = benign prostatic hypertrophy, CA = prostatic carcinoma)

Strain rate	2% pre-compression			4% pre-compression		
	0.4%/s	4%/s	16%/s	0.8%/s	8%/s	32%/s
Normal anterior ($n = 32$)	55 ± 14	62 ± 17	59 ± 19	60 ± 15	63 ± 18	63 ± 16
Normal posterior ($n = 32$)	62 ± 19	69 ± 17	65 ± 18	68 ± 14	70 ± 14	71 ± 11
BPH ($n = 21$)	38 ± 8	36 ± 9	38 ± 8	40 ± 12	36 ± 11	41 ± 13
CA ($n = 28$)	96 ± 19	100 ± 20	99 ± 18	230 ± 34	221 ± 32	241 ± 28

3 THE ELASTOGRAPHIC PROCESS

Several years ago the authors introduced a new method termed *elastography* for direct imaging of the strain and Young's modulus of tissues [24, 51, 52]. Elastography differs from some of the vibrational methods that were described above in several important aspects:

1. The stress applied to the tissue is not vibratory, but rather quasi-static. This tends to avoid problems due to reflections, standing waves and mode patterns which may be set up in the tissue and which may interfere with quality image formation.
2. The applied quasi-static uniaxial stress reduces the complexity of the generalized one-dimensional discrete viscoelastic equation of forced motion of the form

$$M \frac{\mathrm{d}^2 x}{\mathrm{d}t^2} + R \frac{\mathrm{d}x}{\mathrm{d}t} + Kx = F_0 \, \mathrm{e}^{\mathrm{j}\omega t}$$

which contains inertial (M), viscous (R) and stiffness (K) controlled terms, and where x is the displacement, F_0 is the force amplitude and ω is the angular vibrational frequency. The reduced form is the much simpler Hookean equation $Kx = F_0$; since $\omega = 0$ and x is a constant, the velocity and acceleration terms vanish. In principle, this allows the isolation and direct extraction of the local tissue stiffness parameter (K) from measurement of the differential applied force (or stress) F_0 and the resulting local changes in displacement x. For the continuous case, the equivalent equation becomes $\varepsilon E = \sigma$, where ε is the elastic modulus, E is the strain and σ is the applied stress.
3. The average levels of strain produced in the tissue are usually very small (on the order of 0.01). These strain levels are considered small enough to keep the Hookean equation well within the linear range, based on the linear stress–strain relationships for gels and human muscle *in vivo* reported by Mridha and Ödmann [53] which were valid up to a strain level of 0.25. They are kept small also in order to keep the distortion in the time-shifted echo signals (before corrections) to a minimum, hence maintaining a low level of decorrelation noise in the elastogram. If proper corrections can be made, however, it is possible to increase the applied strain and gain in image contrast, to within the limits of the correction methods, and perhaps most importantly.
4. Elastography is capable of producing high-resolution images (elastograms) [24, 27]. The term 'elastogram' is used in this article as a generic descriptor of all the different kinds of images that display some parameters that are related to the elastic behaviour or nature of the tissue. In this sense, elastograms will be described that display axial or lateral strains, the elastic moduli or Poisson's ratio distributions in tissues.

When an elastic medium, such as tissue, is compressed by a constant uniaxial stress, all points in the medium experience a resulting level of longitudinal strain whose principal components are along the axis of compression. If one or more of the tissue elements has a different stiffness parameter than the others, the level of strain in that element will generally be higher or lower; a harder tissue element will generally experience less strain than a softer one. The longitudinal axial strain is estimated in one dimension from the analysis of ultrasonic signals obtained from standard medical ultrasound diagnostic equipment. This is accomplished by acquiring a set of digitized radio-frequency (RF) echo lines from the tissue region of interest by compressing the tissue with the ultrasonic transducer (or with a transducer/compressor combination) along the ultrasonic radiation axis by a small amount (about 1 per cent or less of the tissue depth) and by acquiring a second, post-compression set of echo lines from the same region of interest. Congruent echo lines are then subdivided into small temporal windows which are compared pairwise by using cross-correlation techniques [54], from which the change in arrival time of the echoes before and after compression can be estimated. Due to the small magnitude of the applied compression, there are only small distortions of the echo lines, and the changes in arrival times are also small. The local longitudinal strain is estimated as [24]

$$e_{11,\mathrm{local}} = \frac{(t_{1\mathrm{b}} - t_{1\mathrm{a}}) - (t_{2\mathrm{b}} - t_{2\mathrm{a}})}{t_{1\mathrm{b}} - t_{1\mathrm{a}}}$$

where $t_{1\mathrm{a}}$ is the arrival time of the pre-compression echo from the promixal window, $t_{1\mathrm{b}}$ is the arrival time of the pre-compression echo from the distal window, $t_{2\mathrm{a}}$ is the arrival time of the post-compression echo from the proximal window and $t_{2\mathrm{b}}$ is the arrival time of the post-compression echo from the distal window. The windows are usually translated in small overlapping steps along the temporal axis of the echo line, and the calculation is repeated for all depths. The fundamental assumption made is that speckle motion adequately represents the underlying tissue motion for small uniaxial compressions [55]. Recently, solutions to the inverse problem have been described in the literature [56–58] that are capable of converting estimated tissue displacements and/or strains to modulus elastograms, with the assumed knowledge of the boundary conditions and under several other assumptions. Under the assumption of plane strain state [57] and plane stress state [56] conditions the reconstruction algorithm proposed in references [56] and [57] requires the knowledge of the lateral tissue strains. In reference [57] the lateral strain information was simply derived from the estimated axial tissue strains based on the assumption of tissue incompressibility. In reference [56] only theoretical data derived from the analytical solution of the elasticity equation of an infinite medium embedding a circular inclusion were used to test the reconstruction algorithm. In reference [58] only the

estimated axial tissue displacements are used for the reconstruction. It has also become possible to generate lateral strain elastograms based on incompressibility processing [59] or from direct lateral strain estimations [42]. Poisson's ratio elastograms have also been reported [42].

It is important to emphasize that elastography is a method that ultimately can generate several new kinds of images. As such, all the properties of elastograms are different from the familiar properties of sonograms. While sonograms convey information related to the local acoustic backscatter energy from tissue components, elastograms relate to its local strains, Young's moduli or Poisson's ratio. In general, these elasticity parameters are not directly correlated with sonographic parameters, i.e. elastography conveys new information about internal tissue structure and behaviour under load that is not otherwise obtainable.

The general process of creating strain and modulus elastograms, beginning with the modulus distribution in tissue and ending with a corresponding modulus elastogram, is shown in Fig. 1, showing a block diagram of the process. The input to the process is the intrinsic tissue modulus distribution. The outputs can be either the strain (axial and/or lateral) elastograms, the Poisson elastogram or the modulus elastogram. The tissue strain obtained by a quasi-static tissue compression, restricted by the mechanical boundary conditions, is measured using the ultrasound system. The block describing the *strain filter* [43] embodies the selective filtering of the tissue strains by the ultrasound system and signal processing parameters. The strain filter predicts a finite

dynamic range and respective elastographic signal-to-noise ratio (SNRe) at a given resolution in the elastogram, limited by noise and/or decorrelation. The contributions of the signal processing and ultrasound system parameters and other algorithms are indicated as inputs into the strain filter. The optimized strain elastogram is used as an input to the (optional) inverse problem solution block, where the contrast transfer efficiency (CTE) is improved, with subsequent reduction of artefacts in the modulus elastogram. All these blocks are described later in this article. A complete description may be found in Ophir *et al.* [26].

4 CONTRAST-TRANSFER EFFICIENCY

Using ultrasonic techniques, it is only possible to measure some of the components of the local tissue strain tensor. The local components of the stress tensor remain unknown. If the optional inverse problem solution is not used (e.g. because of incomplete knowledge of the boundary conditions, complexity of the assumptions or computational load), the strain elastogram is all that is available to represent the distribution of tissue elastic moduli. This representation may result in mechanical artefacts and in a limitation of the contrast-transfer efficiency (CTE) [45, 46] under certain conditions. The CTE was defined by Ponnekanti *et al.* [45] as the ratio of the observed (axial) strain contrast measured from the strain elastogram and the underlying true modulus contrast, using a plane strain state model. Expressed in
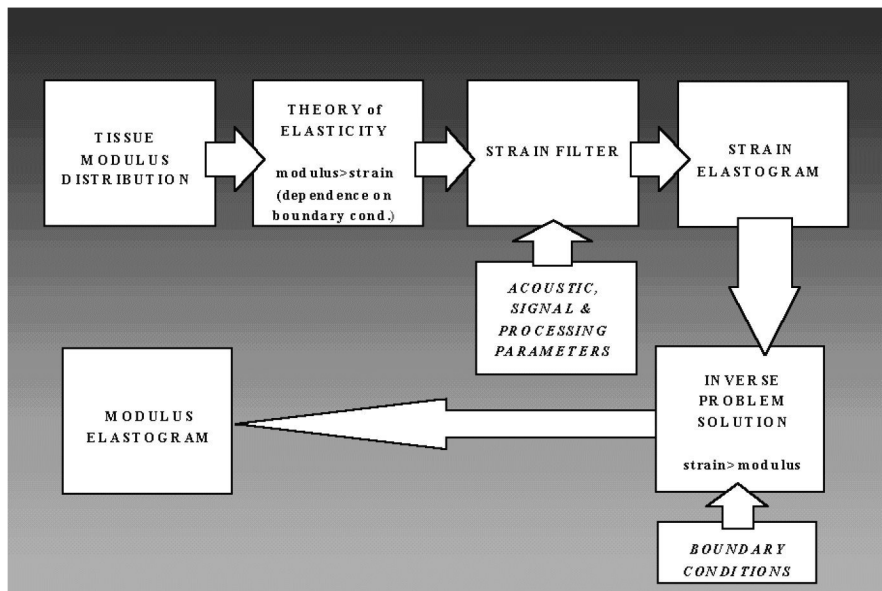

Fig. 1 Block diagram showing the process of generating strain and modulus elastograms from tissues. Note that the production of the modulus elastogram via the inverse problem solution is an optimal enhancement to the process

decibels, it is given by

$$\mathrm{CTE(dB)} = |C_0(\mathrm{dB})| - |C_t(\mathrm{dB})|$$

where the magnitude is used in order to have the CTE normalized to the zero dB level; i.e. the maximum efficiency is reached at 0 dB for both hard and soft inclusions. This property of elastography represents a fundamental limitation that has been verified by finite element (FE) simulations [45] and was also corroborated theoretically by Kallel et al. [46]. Figure 8 in a later section shows the behaviour of the CTE parameter over an 80 dB dynamic range of 'true' modulus contrast as measured from simulated data and as predicted using an analytical model. It is clear from the figure that for low modulus contrast levels (a high level of target modulus homogeneity), the elastographic strain contrast is nearly equal to the modulus contrast (CTE ≈ 1 or 0 dB). This is a very important observation, since it suggests that for low modulus contrast tissues, the simply computed axial strain elastogram itself is nearly proportional to the true modulus elastogram. This expected result has been verified experimentally using *ex vivo* ovine kidneys [11]. Stiff inclusions have a relatively high level of contrast-transfer efficiency. However, soft inclusions that are completely surrounded by harder background material have a low contrast-transfer efficiency, and thus may not be well visualized by elastography. The reason for this limitation lies in the fact that due to the incompressible nature of many soft tissues (Poisson's ratio ∼0.5), the soft inclusion will be so constrained that it will not be able to deform under pressure as it might otherwise do without constraints, thus assuming instead elastic properties that are closer to those of the surrounding stiffer material. Later it will be shown that after considering elastography within the framework of the inverse problem solution, the CTE may be significantly improved.

5 AXIAL STRAIN ELASTOGRAPHY

Elastography is inherently a three-dimensional problem. However, the early elastograms estimated and displayed strains in the axial direction only [24]. Until recently, all the tissue motion in the lateral and elevational directions were ignored. However, recent work by Lubinski et al. [59], Chaturvedi et al. [60, 61] and Konofagou and Ophir [42] have taken into account the non-axial tissue movement, and even used the lateral displacement to compute lateral strain elastograms [42]. In this section, however, it will be assumed that there is no non-axial tissue movement, thus concentrating only on the axial displacement and strain estimation.

5.1 Time delay estimation (TDE) of signals from strained tissues

Time delay is a very important parameter in elastography. The tissue strain is typically estimated from the gradient of tissue displacements. The local tissue displacements are estimated from the time delays of gated pre- and post-compression echo signals [24]. Time delays are generally estimated from the location of the peak of the cross-correlation function between the gated pre- and post-compression echo signals.

The quality of elastograms is highly dependent on the quality of the TDE. TDE in elastography is mainly corrupted by two factors: firstly, the random noise (electronic and quantization) introduces errors in the TDE and, secondly, tissue needs to be compressed to produce elastograms. The very same compression of the tissue distorts the post-compression signal such that it is not an exact delayed version of the pre-compression signal. This decorrelation increases with increasing strain and is independent of the signal-to-noise ratio in the echo signals (SNRs). Any phenomenon (such as lateral and elevational motions) that degrades the precision of the time delay estimates will also degrade the strain estimates, thus introducing additional noise into the elastogram.

5.2 Decorrelation and stretching

Echo signal decorrelation is one of the major limiting factors in strain estimation and imaging. Alam and Ophir [62] have demonstrated that for small strains, temporal stretching [52, 63, 64] of the post-compression signal by the appropriate factor can almost entirely compensate for the axial decorrelation. When the post-compression echo signal is stretched, it in effect realigns all the scatterers within the correlation window. In other words, appropriate temporal stretching removes the mean intra-window strain. Global stretching (of all windows equally) was found to significantly improve the SNRe and expand the strain dynamic range in elastograms. Moreover, this step is computationally not very intensive. Thus, a uniform global stretching of the post-compression A-line prior to the displacement estimation is highly advisable. In low-contrast targets and/or low strains, this is a very efficient displacement estimator. In these situations, it produces quality elastograms without significantly adding to the computational load. However, if the applied strain is large in high-contrast targets, there will be significant overstretching in the areas of low strains, which by itself can significantly degrade elastograms in these areas. However, stretching is mandatory in the presence of large strains; otherwise the elastograms are so noisy that they are practically useless. It also enhances the dynamic range of elastography. It must be remembered that axial stretching can only recover most of the decorrelation suffered due to scatterer motion in the axial direction; decorrelation due to lateral and elevational motions, as well as other sources of decorrelation, cannot be compensated for in this way, and require other methods. Alam et al. [65]

have shown that a deconvolution filtering approach may be useful in reducing the remaining decorrelation that results due to stretching of the point spread function (PSF) when the post-compression echo is stretched.

5.3 Other estimators

5.3.1 Adaptive stretching

Temporal stretching significantly improves TDE in elastography. However, the proper temporal stretching factor is dependent on the local strain, an unknown parameter one is trying to estimate. In an elastically inhomogeneous tissue, the strains will vary and thus, ideally, the stretching factor will have to be varied at different window locations. Since temporal stretching by the factor that compensates for the strain maximizes the correlation, an iterative algorithm is indicated. In this algorithm, the local temporal stretching factor is adaptively varied until a maximum in the correlation is reached. The local strain is then computed directly from this temporal stretching factor. Since the axial correlation is maximized at each data window between the pre- and post-compression A-lines, this estimator is an 'optimal' (one-dimensional) estimator of strain. It is also well known that the gradient operation amplifies noise in the displacement estimates. Since adaptive stretching involves only intra-window operations and no inter-window operation, it does not suffer from this type of degradation. Overall, adaptive stretching may help in improving the elastographic performance by a large factor. Like the uniform global stretching, it also increases the dynamic range of elastography [66].

Figure 2 shows elastograms for various methods discussed in this section for an inhomogeneous tissue-mimicking phantom. The applied strain was 2 per cent. Figure 2a shows the elastogram produced with no stretching. At this strain, the gradient method without stretching fails to produce a useful elastogram due to severe decorrelation. Figures 2b and c show elastograms

produced with uniform stretching and adaptive stretching respectively. Both elastograms have low noise, but the elastogram produced using adaptive stretching appears less noisy. Figure 3 shows the elastograms produced on an *in vitro* ovine kidney that has a thermal lesion in the upper pole. The applied strain was 0.5 per cent. Figure 3a was produced with no stretching and Fig. 3b was produced using adaptive stretching. This last image shows better details and has less visible noise.

5.3.2 Correlation coefficient

It has been discussed how the correlation between the pre- and post-compression echoes can decrease with applied strain. However, decorrelation itself has been used to estimate delay and/or strain. Various researchers used the correlation coefficient to estimate tissue motion
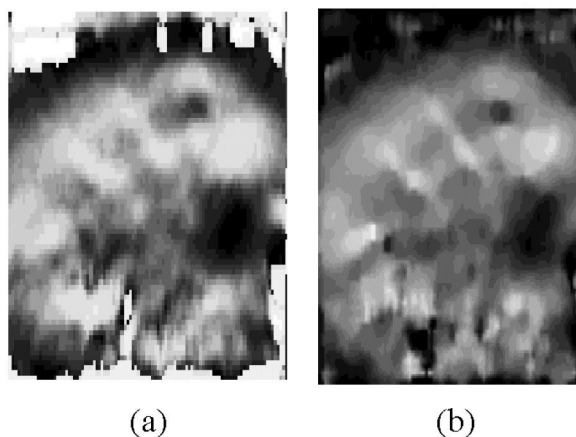
(a)   (b)

Fig. 3 Elastograms of an ovine kidney *in vitro* with an approximately 3 mm diameter induced thermal lesion (black circle) in the upper pole. The applied strain is 0.5 per cent. Window size = 2 mm, window overlap = 50 per cent. Elastograms: (a) conventional gradient method, (b) adaptive stretching. The actual lateral width of each elastogram is 40 mm
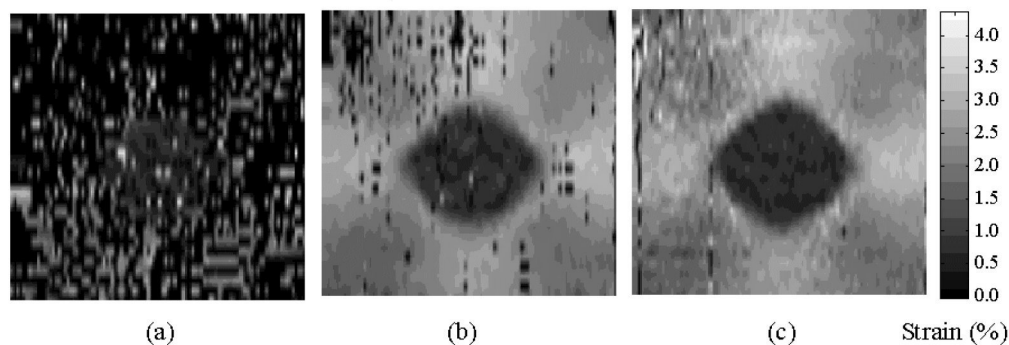
(a)   (b)   (c)   Strain (%)

Fig. 2 Inhomogeneous phantom experiment with 2 per cent applied strain. Window size = 3 mm, window overlap = 50 per cent, no median filtering. Elastograms: (a) gradient, (b) gradient with stretching and (c) adaptive stretching

[67–71]. Bamber and Bush [72] proposed using the decorrelation coefficient (1 minus the correlation coefficient) for the envelope signals for freehand elasticity imaging. Varghese and Ophir [73] have demonstrated that the decorrelation coefficient has poor precision as a strain estimator. Alam and Ophir [74] have demonstrated using simulated data that changes in the centre frequency and SNRs (both the PSF and the SNR vary due to frequency-dependent attenuation, changes in the beam, etc., as the ultrasonic pulse propagates through the tissue) introduce unknown variable bias. Because of its simplicity, this estimator may be a valuable tool for freehand elasticity imaging. However, the disadvantages need to be recognized and care should be taken when using this estimator.

5.3.3   Phase-based methods

It is also possible to use phase to measure small tissue displacements [55], and commercial ultrasound scanners use phase change to estimate motion for Doppler processing. At least one group working on elasticity imaging uses a phase-based displacement estimator [28]. Since the phase is only well defined for narrowband systems, some bandpass filtering is done prior to the computation of the phase, which may introduce a loss in spatial resolution.

5.3.4   Least-squares strain estimator

A least-squares strain estimator (LSQSE) for elastography has been proposed [75]. It was shown that with such an estimator the signal-to-noise ratio in an elastogram (SNRe) was significantly improved due to the reduction of the displacement noise amplification due to the gradient operation. The LSQSE results in an increase of the elastographic sensitivity (the smallest strain that could be detected), thereby increasing the strain dynamic range that is depicted on the elastogram. Using simulated data, it was shown that a trade-off exists between the improvement in SNRe and the reduction of strain contrast and spatial resolution.

5.3.5   Butterfly search

Alam and Parker [76–78] developed the 'butterfly search' technique for complex envelope signals from a deterministic analysis, derived using Schwartz's inequality. Since this method can simultaneously analyse more than two successive A-lines, it is a natural candidate in multicompression elastography. Preliminary results have shown that it may improve the SNR and the dynamic range in elastography.

5.3.6   Direct, incoherent, spectral strain estimators

Elastography has been shown to be capable of producing quality strain images *in vitro* and *in vivo*. Standard elastography uses a *coherent* cross-correlation technique to estimate tissue displacement and tissue strain using a subsequent gradient operator. While coherent estimation methods [24, 28, 29, 63] generally have the advantage of being highly accurate and precise, even relatively small undesired motions are likely to cause signal decorrelation, and thus significant degradation of the elastogram. For elastography to become more universally practical in applications such as intravascular and abdominal imaging, limitations associated with coherent strain estimation methods that require tissue and system stability must be overcome. On the other hand, *incoherent* estimators [79–83] are moderately less precise but far more robust.

The principal idea behind the spectral approach is based on the Fourier scaling property. The previously used spectral method proposed by Talhami *et al.* [79] relates the relative change in the mean coherent scatterer spacing [79, 84–90] to the strain, and uses it for intravascular applications. This method assumes the presence of coherent tissue scatterers as well as underlying tissue periodicities in the tissue structure, which may not hold in most cases. In contrast, the spectral methods presented in this section [82, 83] make no assumptions regarding the composition or distribution of the tissue scatterers.

An important advantage associated with the spectral estimators [82, 83], as with adaptive stretching [66], is that they may be used to estimate strain directly (i.e. without using noise-amplifying gradient operators) within a single estimation window. Tissue strain using the spectral shift can be measured via the spectral centroid shift [82] or spectral cross-correlation [83]. The spectral centroid [91–94] has been widely used in estimating the Doppler shift, attenuation [91] and backscattering [94]. While the downshift in the spectrum with frequency-dependent attenuation complicates the estimation process for the Doppler shift, in elastography this problem is not encountered since differential estimates are used, which suffer common frequency-dependent attenuation effects. The upshift in the centre frequency estimate with strain is illustrated with a simulation in Fig. 4.

For the spectral strain estimator using the centroid shift [82], it is found that if the bandwidth of the scattering noise process is much larger than the bandwidth of the system PSF, then

$$\frac{f_{c2} - f_{c1}}{f_{c1}} \cong As$$

where the strain estimate is equal to the fractional shift in the centre frequency of the power spectra, f_{c1} and f_{c2}, of the pre- and post-compression signals respectively within a scaling constant A. In the case of spectral cross-correlation [83], the ratio of the spectral shift, which was measured using cross-correlation of the spectra, to the centre frequency of the PSF is proportional to the tissue strain. Interestingly, this equation is of the same form
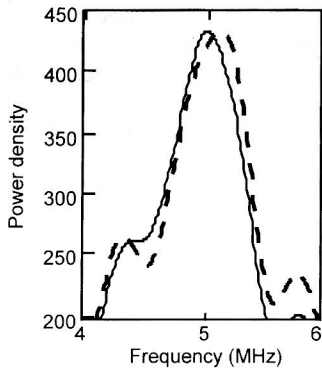
Fig. 4 The frequency centroid shift due to strain: example of 1 per cent compressive tissue strain. The peak of the power spectrum (solid line), which in this case is very close to the actual centroid, is upshifted (broken line) due to the applied compressive strain
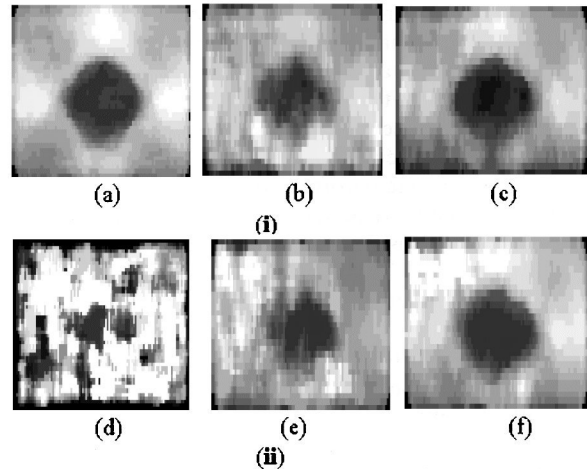

Fig. 5 Elastograms obtained using coherent and incoherent strain estimation algorithms, for a phantom with an inclusion that is three times stiffer than the background. The RF signals were obtained using a 7.5 MHz linear array with a 50 per cent bandwidth. The elastograms were obtained using (i) 0.5 per cent and (ii) 3 per cent applied compression. (a and d) Elastogram obtained using the coherent cross-section method. (b and e) Elastogram obtained using the centroid method. (c and f) Elastogram obtained using the spectral cross-correlation method

as the defining equation for the strain itself, which is given as

$$\frac{L_1 - L_0}{L_0} = s$$

where L_0 is the original length of the segment and L_1 the new length after compression. Comparison of the estimation performance using coherent cross-correlation and the direct spectral strain estimators are illustrated qualitatively in Fig. 5 using elastograms obtained from an inhomogeneous experimental phantom containing an inclusion three times stiffer than the background at both low (0.5 per cent) and high (3 per cent) applied strains [82, 83]. Note that coherent strain estimation provides the least noisy elastogram for the low compression of 0.5 per cent [Fig. 5(i)], when compared to the spectral methods. However, for the large applied compression of 3 per cent [Fig. 5(ii)], the coherent strain estimator fails when compared to the spectral methods that produce reasonable elastograms. No stretching techniques were used. Finally, the method of spectral cross-correlation provides the least noisy elastogram in this case [83].

5.4 Options in the treatment of non-axial motions

When tissue is compressed, in addition to the axial motions it also undergoes non-axial motions that introduce additional decorrelations [95]. There are various ways to handle this problem:

1. Use small compression steps (typically <1 per cent applied strain). This reduces the motion of the scatterers in the lateral and elevational directions, and thus scatterers do not move substantially in and out of the beam. It is also possible to perform strain imaging by averaging the elastograms over a number of small applied strain increments [28, 96]. Varghese and Ophir [97] have shown that in multicompression

elastography there exists an optimal incremental applied strain that maximizes the achievable SNRe.
2. The tissue can be mechanically confined to reduce lateral motion. This increases the elevational motion, but since the beam is broader in that direction, its effect can be neglected for the most part [95].
3. Use incompressibility processing, originally proposed for modulus reconstruction purposes [59], where the lateral strains are computed from the axial strains under certain assumptions. However, this method assumes Poisson's ratio to be 0.5, which may not always be true [53], and the contour of the zero lateral displacement must be accurately estimated.
4. Use a method to correct for non-axial motion. Chaturvedi et al. [60, 61] have proposed a companding method that reconstructs the pre-compression sonogram by compensating for lateral motion. Konofagou and Ophir [42] have proposed a method that can estimate the lateral displacement with high precision and produce excellent corrected axial and lateral strain elastograms. This approach will be briefly discussed in the next section.

6 LATERAL STRAIN ELASTOGRAPHY

A major disadvantage of the current practice of elastography is that only the axial component of the strain

tensor is used to produce the elastogram, while the lateral and elevational components are basically disregarded. However, all three components are needed to fully characterize the motion of a three-dimensional target [98]. Furthermore, the lateral and elevational components can severely corrupt the axial strain estimation by inducing decorrelation noise [98, 99]. A new method has therefore been developed that produces *high precision* lateral displacements [42]. In reference [42] it is shown that the higher the interpolation scheme, the higher the number of independent displacement estimates and thereby the higher the precision of the estimation. Due to this high precision lateral tracking, quality *lateral* elastograms can be generated that display the lateral component of the strain tensor. The main requirements on the transducer specifications are: (a) a minimum of 50 per cent overlap between adjacent beams and (b) a well-focused beam (on the order of 1 mm). Preliminary studies [42] have shown that the precision increases with a beamwidth decrease (possibly due to the subsequent improvement in the ultrasonic lateral resolution) and this constitutes a topic of current investigations. Briefly, the new method works as follows. Interpolated post-compression A-lines are generated via a method of weighted interpolation [42] between neighbouring A-lines. Then, pre-compression segments are cross-correlated with original and interpolated post-compression segments [42] and the location of maximum correlation indicates the amount of lateral displacement that resulted from the compression. A least-squares algorithm [75] is used to derive the lateral strain from the lateral displacement information.

A correction for lateral motion has been described by Chaturvedi *et al.* [61] using a block-matching technique described by Bohs and Trahey [100]. The correction results in a significant increase of both the signal-to-noise ratio and dynamic range of the axial elastogram at large applied strains. This is similar in principle to the one-dimensional axial motion compensation and stretching described by Céspedes and Ophir [63] as a means for reducing the noise in elastograms. Taking into account the coupling between axial and lateral motion, an iterative method has been developed of successive corrections for and estimations of axial as well as lateral motion [42]. This led to a consistent increase of the signal-to-noise ratio of both axial and lateral elastograms. Results of the iterative method are shown in Figs 6 and 7 from finite element simulations and *in vitro* prostate data respectively [42]. Figure 6 shows that the technique is able to remove large ('curtain noise' near the edges of the image) as well as smaller (close to the centre of the image) decorrelation effects due to lateral motion, which are responsible for poor contrast-to-noise ratios for the hard lesion. This kind of improvement was predicted by Kallel *et al.* [99] via the calculation of the corresponding theoretical strain filters. In a similar fashion, the axial and lateral elastograms of the prostate *in vitro* (Fig. 7)

show consistent improvement following the corrections. The part of the axial elastogram in Fig. 7c most corrupted by correlation noise coincides with the part of the maximum lateral displacement in Fig. 5d. This, along with the corrected axial elastogram of Fig. 7f, verifies the assumption that the decorrelation noise unaccounted for in Fig. 7c is due to lateral motion. From Figs 7e and f it may be concluded that axial and lateral elastograms are different due to existing compressibility and/or anisotropy in the prostate tissue. In a later section (Section 8) a method is proposed to measure compressibility through calculation of the local Poisson ratio. The iterative method has also been proven to be useful in breast data *in vivo* [42].

7   MODULUS ELASTOGRAPHY

Elastography based on quantitative strain imaging suffers from mechanical artefacts (shadowing and target hardening artefact [24]) and from limitations to the contrast-transfer efficiency (CTE). To go beyond such presumed limitations, a few groups independently considered elastography as a new, challenging inverse problem [56–58, 101]. The inverse problem (IP) approach is used extensively in electromagnetics, optics and geophysics research [102]. In the biomedical field it has been extensively studied in bioelectricity to determine the distribution of potentials on the surface of the heart or the brain from a limited number of peripheral potential measurements. However, it is relatively new in the field of continuum mechanics [103–105] and until recently it was not applied in the field of biomechanics, to which elastography belongs.

For many reasons (non-linearity, noise in the data, lack of complete data set, etc.), most of the IPs are ill-posed in the sense of Hadamard [106]. Therefore, finding a unique and stable solution of an IP is very difficult. To this end, during the second half of this century, many techniques have been proposed [107]. Since these techniques usually require several big matrix inversions, they remain complex, consuming computer time and memory. In elastography it is fortunate that the solution of the IP is an option rather than a necessity (Fig. 1) unlike in many other fields. Conceivably, the exercise of this option will be restricted to cases where the simple strain images alone are not sufficient to adequately complete a given task (detection, characterization, etc.). Below is a short summary of the different techniques proposed to solve the IP in elastography, followed by typical results obtained using the technique of Kallel and Bertrand [101]. The simulation results of the elastic modulus reconstruction were obtained after a total of 10 iterations of the linear perturbation technique proposed in reference [101].

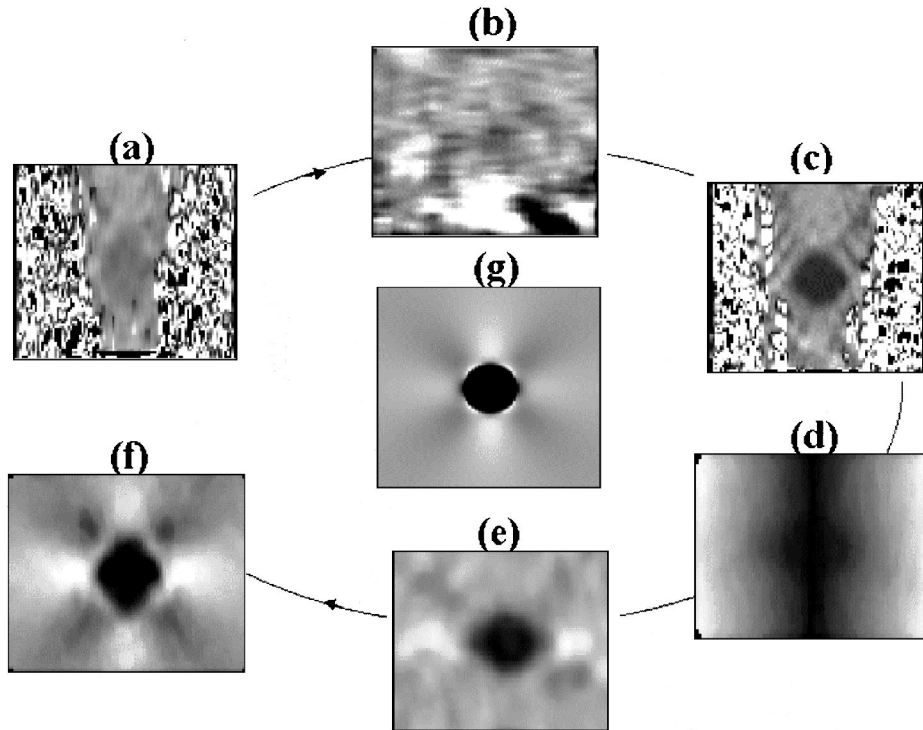The approach proposed by Skovoroda *et al.* [57] and

Fig. 6 Finite element plane strain state simulation of an inclusion twice harder than the embedding background (modulus equal to 21 kPa) at 3 per cent axial compression: (a) first axial elastogram (no axial or lateral correction), (b) first lateral elastogram (no axial correction), (c) second axial elastogram (with axial correction, no lateral correction, note the existence of 'curtain noise' resulting from unaccounted-for high lateral displacement towards the lateral sides of the target), (d) lateral displacement image (with axial correction), (e) second lateral elastogram (with axial correction), (f) third axial elastogram (with axial and lateral corrections) and (g) true axial strain image obtained from finite element simulation

Sumi *et al.* [**56**] to solve this problem consisted of rearranging the equations of the forward problem so that the tissue elastic modulus distribution is the unknown, while the strain and displacement fields are known. With this method, all the components of the strain/displacement tensors must be known. The technique proposed by Kallel and Bertrand [**101**] is based on the use of a linear perturbation method. It consists essentially of minimizing the least-squares error between the observed and predicted displacement fields. The predicted displacement field is obtained using a theoretical model of the elasticity equations (constitutive equations). In this technique both the force distribution under the compressor and the measured axial displacement field are used for the reconstruction of the modulus distribution. When the force distribution is unknown, a penalty technique may be used [**108**]. Using computer simulations, Kallel [**58**] has shown that solving the inverse problem in elastography reduces the inherent strain artefacts, and results in a significant improvement of the CTE. This is illustrated in Fig. 8, which shows

reconstruction results obtained under ideal conditions, where the boundary conditions are perfectly known and noiseless displacement data are used for the reconstruction. Nevertheless, the displacement data are corrupted by random noise resulting from numerical errors induced when the forward problem is solved using the FE technique. Since in practice the data are noisier (due to decorrelation noise) and the boundary conditions are generally not completely known, all modulus reconstruction techniques will also have their own limitations and artefacts [**108**]. To date, no systematic comparison of modulus reconstruction to simple strain imaging has been conducted. It is expected from CTE analysis, however, that the importance of the reconstruction algorithms may be greater in tissues with high stiffness contrast and lesser in situations where low contrast is encountered, such as in normal tissues.

Figure 9a shows an example of a relatively complex simulated modulus distribution. It consists of a homogeneous background embedding three hard lesions: two of them are 3.5 times harder than the background and
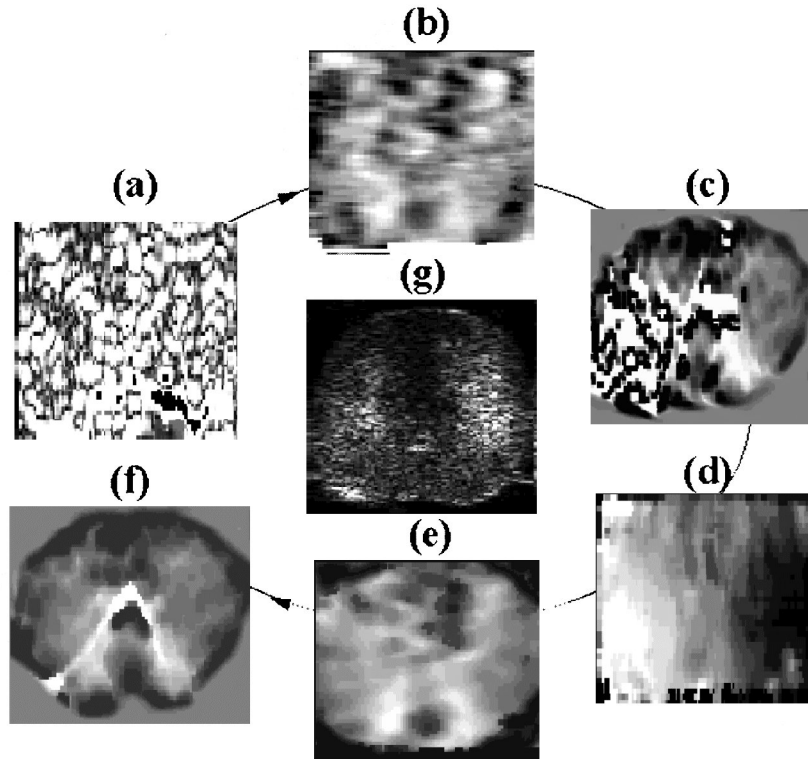
Fig. 7　*In vitro* anterior–posterior view of a canine prostate at 2 per cent axial compression (elevationally confined): (a) first axial elastogram (no axial or lateral corrections), (b) first lateral elastogram (no axial correction), (c) second axial elastogram (with axial correction, no lateral correction), (d) lateral displacement image (with axial correction), (e) second lateral elastogram (with axial correction), (f) third axial elastogram (with axial and lateral corrections) and (g) sonogram (i.e. envelope of the RF sonographic data)

the third one is 4 times harder than the background. Figure 9b shows the axial strain distribution resulting from the application of a uniform axial pressure on the top of the tissue block while assuming perfect non-slip boundary conditions at the upper and lower surfaces of the tissue. Figure 9c shows the same axial strain distribution but obtained using a higher density finite element mesh (3500 elements instead of 1400 elements). Observe that the increase in the number of elements significantly reduces the numerical errors. This is achieved with a considerable increase in computer time and memory. For the reconstruction, the coarse finite element mesh is usually used since the present algorithm involves matrix inversion. Both strain images clearly depict the three lesions, even in the presence of the bright artefacts resulting from the inherent stress concentrations. As shown in Figs 9d and e, the artefacts of the strain image are completely removed when the uniform pressure is used as a boundary condition. However, when the uniform displacement is used as a boundary condition, the shadowing artefact of the strain image is replaced by another artefact consisting of the projection of the lesions towards the upper and lower surfaces of the tissue

block. This artefact is due to the use of the penalty technique, which assumes a pressure that is uniformly distributed at the upper surface of the tissue block [**58, 95**].

As shown by the example of Fig. 9, in the case of a relatively simple arrangement of elastic inhomogeneities, the axial strain image alone is sufficient for detection purposes. However, in more complex situations it is expected that the strain image alone may not be sufficient even for the simple task of detection. To illustrate this, the reconstruction of the simulated modulus distribution shown in Fig. 10a is considered. This modulus distribution is obtained by randomly changing the value of Young's modulus of 25 per cent of the total number of the elements of the FE mesh (each element was set to be 3 times harder than the background). As shown in Fig. 10b, the strain image does not depict the individual elastic inhomogeneities without ambiguity. However, many of these are depicted by the reconstructed modulus distribution (Fig. 10c). Notice that in this complex situation the reconstruction is not perfect even when the boundary conditions are completely known. This is a limitation of the algorithm, and in principle a perfect reconstruction may be possible using an improved algorithm.
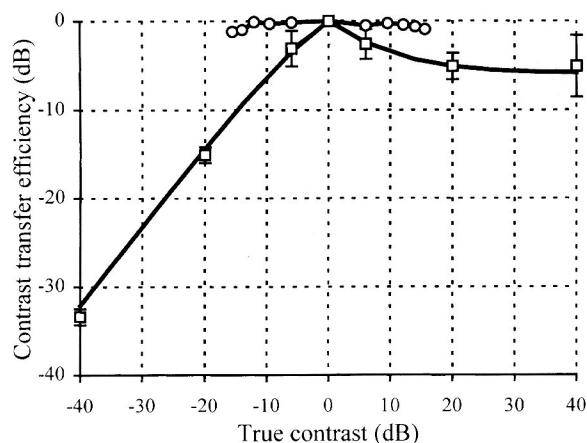
Fig. 8 Contrast-transfer efficiency curve. The zero dB ordinate is the ideal contrast-transfer efficiency. Observe the close match between theory and simulation: (———) predicted observed contrast-transfer efficiency (from Kallel *et al.* [**46**]), (—□—) contrast-transfer efficiency measured from simulated elastograms (from Ponnekanti *et al.* [**45**]), (—○—) contrast-transfer efficiency after solving the inverse problem in elastography as obtained using FE simulation (from Kallel [**58**])

8 POISSON'S RATIO ELASTOGRAPHY

Poisson's ratio (ν) for a plane strain state under uniaxial stress conditions is defined as

$$\nu = -\frac{\varepsilon_1}{\varepsilon_a} \tag{1}$$

where ε_1 and ε_a are the lateral and axial strains respectively. Poisson's ratio is an important mechanical parameter that describes the degree of material compressibility, or the change in volume following an applied compression. Poisson's ratio equals 0.5 for totally incompressible materials and 0 for totally compressible ones. By measuring and imaging the distribution of Poisson's ratio in tissues, it may be possible to estimate the amount of relocatable water contained in different tissue regions [**109**].

From the definition of Poisson's ratio [equation (1)], it is possible to produce a new image that displays the spatial distribution of Poisson's ratios in the tissue, namely the Poisson's ratio elastogram, or *Poisson elastogram* [**42**], by simply dividing the negative of the lateral elastogram by the axial elastogram. Figures 11 and 12 show simulation results of the axial, lateral and Poisson elastograms for cases without and with Poisson's ratio contrast respectively. In cases where there is a strain contrast between an inclusion and the background, the Poisson elastogram is able to indicate whether that strain contrast (on the axial and lateral elastograms) is due to
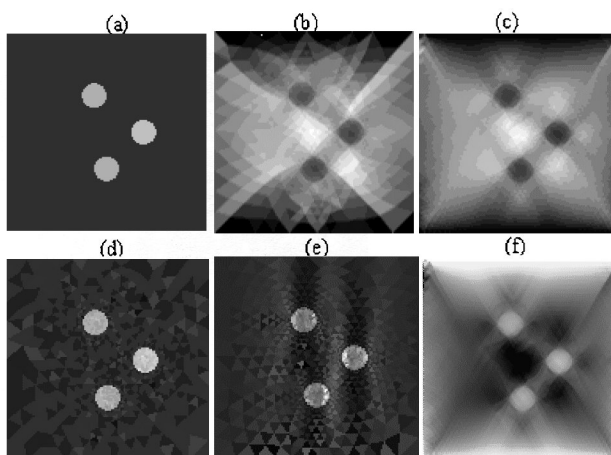

Fig. 9 Simulated elastic modulus distribution and corresponding axial strain and reconstructed images obtained for both force and displacement boundary conditions. (a) Cross-section from the simulated modulus distribution. The size of the ROI is 40 × 40 mm². The homogeneous medium is embedding three circular (5 mm diameter) inclusions; the left two upper and lower inclusions are 3.5 times harder than the background and the right one is 4 times harder than the background. (b) Axial strain image when a constant pressure is used as boundary conditions obtained for a coarse FE mesh. (c) Axial strain image obtained for a finer FE mesh. (d) Reconstructed modulus distribution when uniform pressure is used as boundary conditions. (e) Reconstructed modulus distribution when uniform surface displacement is used as boundary conditions. (f) Inverse of panel (c). Note the various forms of aretfacts shown in the images

a Poisson's ratio contrast, elastic modulus contrast or both.

Poisson elastograms may have interesting applications in assessing the degree of unbound water content in tissues [**110**]. The Poisson elastogram or the time sequence of Poisson elastograms may be used for quantitative assessment and imaging of fluid transport in local regions of oedema, inflammation or other hydrated poroelastic tissues [**111**]. Another interesting and potentially very useful property of the Poisson elastogram is that, as long as the tissue isotropy assumption holds, mechanical stress concentration artefacts due to geometrical boundary conditions should cancel out (Fig. 12c). This means that unlike earlier methods for quantifying tissue fluid transport that were highly dependent on the geometry [**111**], it may be possible to produce images of this basic tissue parameter that are free from geometrical artefacts. Finally, the knowledge of both lateral strain and Poisson's ratio in addition to the axial strain is in general necessary for reconstruction algorithms [**56, 57, 108**]; this implies that the final modulus elastogram could become more accurate if the lateral and Poisson elastograms are computed first.
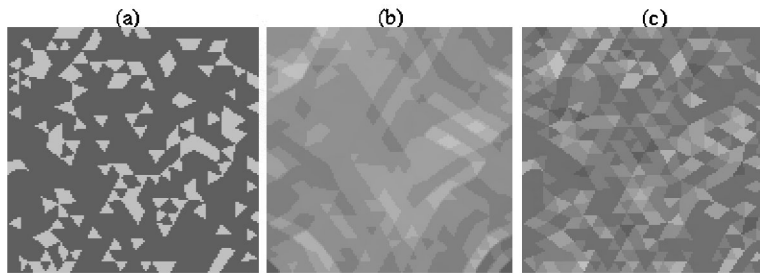
Fig. 10 Simulated elastic modulus distribution and corresponding axial strain image and reconstructed modulus image obtained for uniform applied force boundary conditions. (a) Original modulus distribution. The brighter areas are 3 times harder than the background. (b) The inverse of the axial strain image. (c) Reconstructed modulus distribution
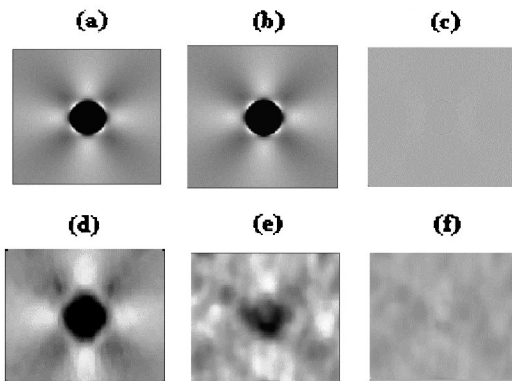

Fig. 11 *True*: (a) axial strain image, (b) negative of lateral strain image, (c) Poisson's ratio image. *Estimated*: (d) axial elastogram, (e) negative of lateral elastogram, (f) Poisson elastogram for a Young's modulus contrast of two and a Poisson's ratio contrast of one. Note how the uniformity of the Poisson elastogram denotes the lack of Poisson's ratio contrast between the inclusion and the background

Fig. 12 *True*: (a) axial strain image, (b) negative of lateral strain image, (c) Poisson's ratio image. *Estimated*: (d) axial elastogram, (e) negative of lateral elastogram, (f) Poisson elastogram for a Young's modulus contrast of two and a Poisson's ratio contrast of 1.65. In this case, the Poisson elastogram shows that the strain contrast in the strain elastograms is also due to the Poisson's ratio contrast, possibly revealing different poroelastic properties between the inclusion and the background

9 THE STRAIN FILTER

The elastographic system has been characterized using both theoretical [43, 44] and experimental [112] methods. Recently, a general theoretical framework referred to as the strain filter (SF) was proposed by Varghese and Ophir [43]. The SF describes the relationship among the resolution, dynamic range (DRe), sensitivity (Smin) and elastographic SNR (SNRe), and may be plotted as a graph of the upper bound of the SNRe versus the strain experienced by the tissue, for a given elastographic axial resolution as defined by the data window length at a fixed overlap. The SF is a statistical upper bound of the transfer characteristic that describes the relationship between actual tissue strains and the corresponding strain estimates depicted on the elastogram. It describes the filtering process in the *strain domain*, which allows quality elastographic depiction of only a limited range of strains from tissue. This limited
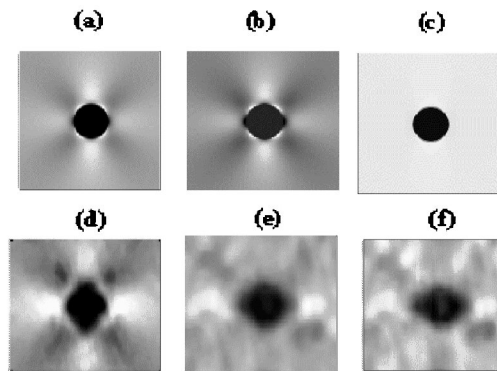
range of strains is due to the limitations of the ultrasound system and of the signal processing parameters. The SF is obtainable as the ratio between the mean strain estimate and the appropriate lower bound on its standard deviation. The SF may be derated due to effects such as tissue attenuation [113] and speckle decorrelation due to undesired lateral tissue motion [99]. The SF is based on well-known lower bounds on the TDE variance, presented in the literature [114, 115]. The low-strain behaviour of the SF is determined by the variance as computed from the Cramér–Rao lower bound (CRLB) (modified for partially correlated signals [116]); the high-strain behaviour of the SF is determined by the rate of decorrelation of a pair of congruent signals due to tissue distortion, as shown in Fig. 13. Figure 14 illustrates the general appearance of the SF, demonstrating the trade-offs among SNRe and resolution for all strains. An important extension to the SF is its combination with the CTE
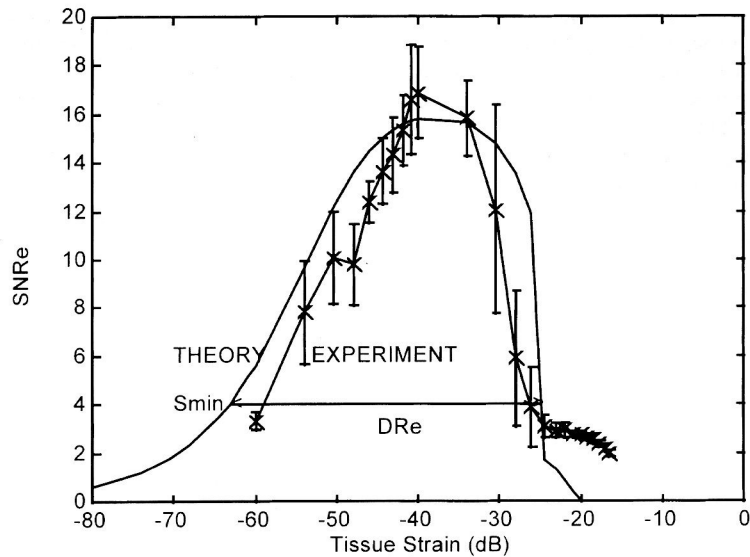
Fig. 13 The theoretical strain filter (SF) [43] along with the experimental strain response (ESR) [112] obtained with ($\times$–$\times$–$\times$) global temporal stretching. The ESR is obtained around a small region (1 cm) around the focus of the transducer from 2 to 3 cm in the elastographic phantom. The ESR and SF are computed using a transducer with a 5 MHz centre frequency and 60 per cent bandwidth, using a window length (Z) of 3 mm with a 50 per cent overlap between data segments. The strain estimates for the ESR is computed from 20 independent experimental realizations of the RF pre- and post-compression signals. DRe is the strain dynamic range measured at the SNRe = 4. Smin is the sensitivity, defined as the lower strain bound of the DRe
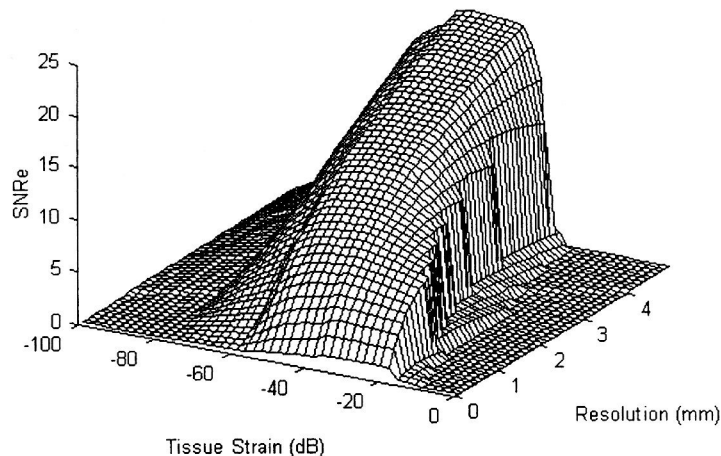

Fig. 14 The general three-dimensional appearance of the SF, showing the trade-offs among strain dynamic range and sensitivity, elastographic SNRe and resolution (defined here as the window length at a fixed overlap). It is generally convenient to plot a cross-section of the three-dimensional SF at a fixed resolution and refer to this cross-section as the SF; the theoretical SF curve of Fig. 13 is an example

formalism to produce elastographic contrast-to-noise ratio (CNRe) versus strain curves (Fig. 16) [117]. This allows the description of the CNRe of simple elastic inclusions or layers in terms of both the mechanical strain contrast limitations in the target and the noise properties of the apparatus. The authors have recently

demonstrated, using a controlled simulation experiment, that the axial resolution may be expressed as a bilinear function of window size and window shift, the latter being more important [118].

The elastographic system is characterized experimentally by estimating the strain response of the system using

an homogeneous uniformly elastic phantom [112]. The experimental strain response (ESR) is evaluated by subjecting the uniformly elastic phantom to a wide range of input strains while computing the accuracy and precision of the estimated strain. The plot of the SNRe estimate versus the estimate of the strain incurred in the phantom over the entire range of compressions generates the ESR, as illustrated in Fig. 13.

The ESR will in general vary with the use of different ultrasound scanners, boundary conditions associated with the experiment and the strain estimation algorithm used. The accuracy and precision of the strain estimation algorithm depends on the transducer used to scan the phantom. In addition, accurate tracking of the scatterer motion is obtained around the focus of the transducer when compared to either the near- or far-field regions of the transducer. For an elastically homogeneous isotropic phantom, when the scan plane is on the axis of symmetry of the phantom in the elevational direction, the motion of the scatterers out of the scan plane is minimized (along the axis of symmetry the scatterers move only in the axial direction under the conditions described above). In addition, the ultrasound beam along the elevational direction is broader, allowing scatterers to stay longer within the beam during compression. It is for this reason that the characterization of the elastographic system is performed along the axis of symmetry of the phantom. The optimal ESR of the elastographic system is therefore obtained at the focus of the transducer and along the scan plane containing the axis of symmetry of the elastographic phantom. The ESR at any other position in the phantom is affected by boundary conditions, lateral and elevational signal decorrelation and the attenuation properties of the phantom.

The SF allows the design and synthesis of elastographic systems [43, 44], while the ESR allows an evaluation of noise performance of any elastographic system [112]. The SFs illustrated in this paper incorporate the use of uniform temporal stretching for strain estimation. Bilgen and Insana [119–121] also derived theoretical closed-form expressions for the strain variances using a Taylor's series expansion. Their method uses a noise figure analysis (ratio of the SNRe to SNRs), and when plotted as a function of applied strain it is similar to the SF. However, these expressions are valid only in cases of non-ambiguous detection of the cross-correlation peak.

9.1 Theoretical framework

A criterion that quantitatively measures the accuracy and precision of the strain estimate is the SNRe [46, 63], defined by

$$\mathrm{SNRe} = \frac{m_s}{\sigma_s} \qquad (2)$$

Here m_s denotes the statistical mean strain estimate and σ_s denotes the standard deviation for the strain noise estimated from the elastogram. When the statistical mean value of the strain is replaced by the ideal tissue strain, and the minimum standard deviation by the theoretical lower bound on the standard deviation, an upper bound on the performance of the strain estimator is obtained, referred to as the strain filter [43]:

$$\mathrm{SNRe}^{\mathrm{UB}} = \frac{s_t}{\sigma(\hat{s})_{\mathrm{ZZLB}, \rho}} \qquad (3)$$

where s_t is the tissue strain and $\sigma(\hat{s})_{\mathrm{ZZLB}, \rho}$* is the modified Ziv–Zakai lower bound (ZZLB) [122, 123] on the standard deviation of the strain estimator. The ZZLB provides the tightest lower bound for the displacement estimator. The modified ZZLB expression for the strain estimation variance [43, 44] is complicated, and is not reproduced here.

9.2 Non-stationarity of the strain filter

Estimation of tissue strains is inherently a non-stationary process, since the pre- and post-compression RF echo signals are jointly non-stationary (due to signal deformation caused by straining tissue). However, the pre- and post-compression signals can be assumed to be jointly stationary if the tissue strain is estimated using small windowed data segments in conjunction with temporal stretching of the post-compression signal. Frequency-dependent attenuation adds additional (axial) non-stationarity into the strain estimation process versus depth [113], while lateral and elevational signal correlation introduce non-stationarities in the strain estimation process along the lateral and elevational directions respectively [99]. The effect of these non-stationarities on the elastogram can be predicted by the SF (Fig. 15). For example, the effect of lateral decorrelation contributes predominantly to the non-stationary variation in the SNRe [95, 99]. Both the SNRe and the dynamic range are reduced with an increase in lateral decorrelation. As long as any stationary or non-stationary noise source can be described, its effect may be incorporated into the strain filter formalism, resulting in a more realistic, derated strain filter [99, 113].

9.3 Contrast-to-noise ratio in elastography

The contrast-to-noise ratio in elastography (CNRe) is an important quantity which is related to the detectability of a lesion [117]. The properties of the ultrasound

---

* The lower bounds on the strain estimation variance are denoted with an additional subscript ρ to illustrate that these variances are computed for partially correlated signals. These lower bounds converge to the classical bounds when $\rho = 1$.
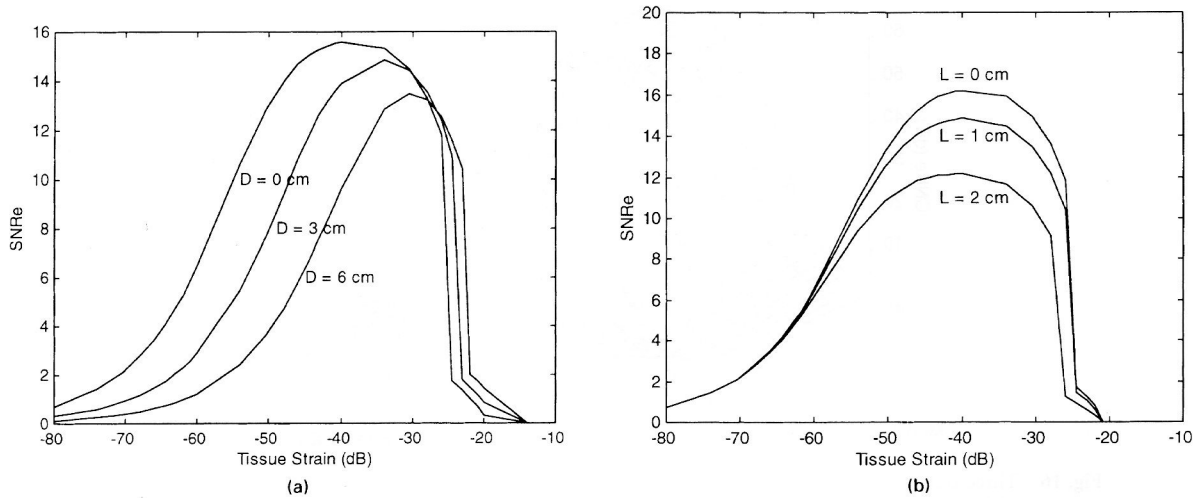
Fig. 15 (a) The non-stationary evolution of the strain filter with linear frequency-dependent attenuation. The bandwidth remains constant with depth. However, the downshift of the centre frequency and the reduction in the SNRs with depth causes the derating in the SF. Note the progressive narrowing of the SF (both in width and height) with depth (increasing frequency-dependent attenuation). The centre frequency downshift induces the shift in the SF towards higher strains, as observed with increasing depths, while the reduction in the SNRs contributes to the dramatic reduction in the dynamic range and sensitivity. (b) Non-stationary variation in the SF for different lateral positions along the transducer aperture and away from its centre. Lateral decorrelation increases with an increase in the beam lateral position (increased lateral tissue scatterers motion), reducing the strain estimation performance with lateral position

imaging system and signal processing algorithms described by the SF can be combined with the elastic contrast properties (CTE) of tissues with simple geometries, enabling prediction of the elastographic contrast-to-noise ratio (CNRe) parameter. This combined theoretical model enables prediction of the CNRe for simple geometries such as layered (one-dimensional model) or circular lesions (two-dimensional model) embedded in a uniformly elastic background. An upper bound on the CNRe [117] is obtained using

$$\text{CNRe} = \frac{2(s_1 - s_2)^2}{\sigma_{s1}^2 + \sigma_{s2}^2} \qquad (4)$$

The CNRe for specific geometries that possess an analytic or experimental CTE description can be obtained by substituting the strains obtained using the elasticity model and their respective variances from the SF into equation (4).

Figure 16 illustrates the general appearance of the upper bound on the CNRe, demonstrating the trade-offs among CNRe and modulus contrast for all applied strains [117]. Note from Fig. 16 and equation (4) that the highest values of the CNRe are obtained where two conditions are satisfied: firstly, the differences in mean strain values must be large and, secondly, the sum of the variances of the strain estimates should be small. The improvement of the CNRe at low modulus contrasts is primarily due to the small strain variances, while at high

modulus contrasts the improvement in the CNRe is due to the large difference in the mean strains. Note from the three-dimensional visualization of the CNRe curves in Fig. 16 that when the differences in the mean strain values are small (the region around the middle of the graph at low contrasts), the CNRe value obtained is almost zero. In addition, the regions with large strains (corresponding to large variances in the strain estimate due to signal decorrelation) also contribute to low CNRe values. Knowledge of the theoretical upper bound on the CNRe in elastography is crucial for determining the ability to discriminate between different regions in the elastograms. The CTE for the elasticity models and the elastographic noise characterized by the SF determine the CNRe in elastography. The three-dimensional visualization of the CNRe curves illustrates the strain dependence of the CNRe [117]. The three-dimensional plot provides a means of maximizing the CNRe in the elastogram for the given ultrasound system and signal processing parameters.

Figures 17a and b show two-dimensional cross-sectional cuts of Fig. 16 as well as simulation and experimental measurements at a fixed applied strain (1 per cent) and a fixed modulus contrast (−10 dB) respectively. Figure 17a compares the behaviour of the upper bound of the CNRe using both one- and two-dimensional models for the tissue geometries. For the one-dimensional model, strain is modelled by considering an
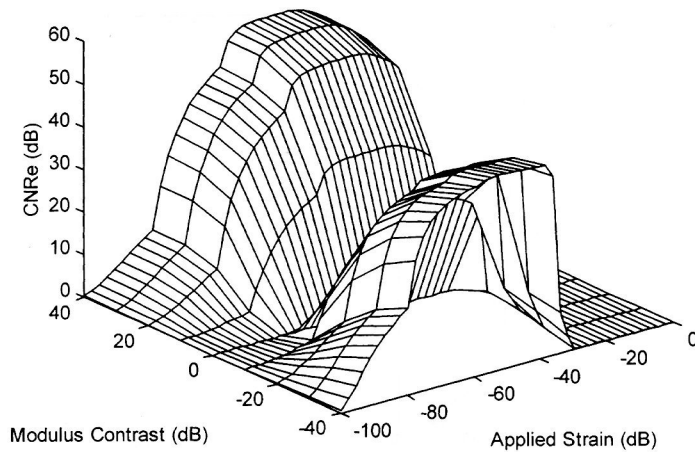
Fig. 16 Three-dimensional plot of the CNRe curves, illustrating the variation in the upper bound of the CNRe with the modulus contrast with varying applied strains for the two-dimensional tissue elasticity model. The curves were obtained using a transducer with a 7.5 MHz centre frequency with a 60 per cent bandwidth and a window length $Z = 2$ mm with a 50 per cent overlap in the data segments

equivalent one-dimensional spring system [**52**], while the two-dimensional analytic solution is used for the two-dimensional model [**46**]. In addition, observe that the simulation and theoretical results follow a similar trend. Note that for soft lesions, the increased signal decorrelation that occurs at large contrasts using the one-dimensional model drastically reduces the CNRe. However, due to the geometry of the two-dimenional

model (soft lesion within a hard background), the strains within the lesion are quite small, even at large contrasts. In the case of hard lesions, one- and two-dimensional models provide similar results. Using the two-dimensional model, a difference of about 10 dB can be observed in the CNRe between the soft lesion and the hard background due to the lower value of the CTE. Note that the suboptimal CTE for soft lesions in the
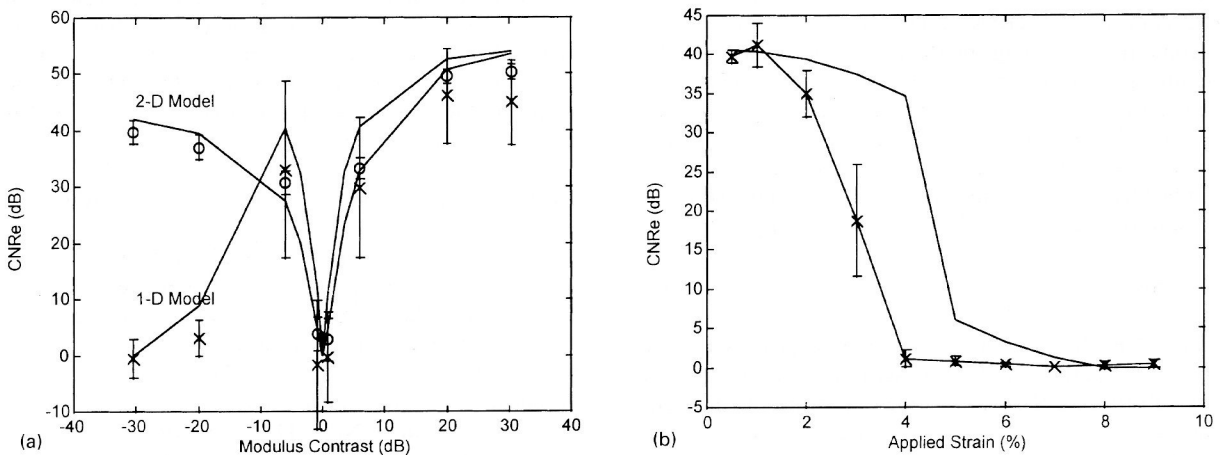

Fig. 17 (a) Theoretical and simulation results illustrating the variation in the CNRe with contrast for a 1 per cent applied strain for the one-dimensional ($\times$) and two-dimensional ($\bigcirc$) tissue models. The graphs with the error bars and symbols denote the simulation results. The same parameters as in Fig. 16 were used. (b) Theoretical (solid line) and experimental ($\times \times \times$) results illustrating the variation in the CNRe with applied strain using a phantom with an inclusion that is three times stiffer than the background. The theoretical results are derated for strain estimation at the edges due to lateral signal decorrelation (20 mm lateral position). The CNRe is computed between a region within the inclusion and the background regions (the four corners of the elastogram shown in Fig. 2). The error bars represent the CNRe variation about these four estimates. The curves were obtained using a transducer with a 7.5 MHz centre frequency and a 60 per cent bandwidth, and using a window length $Z = 3$ mm with a 50 per cent overlap in the data segments

two-dimensional model is responsible for the improvement of the CNRe when compared to the one-dimensional model. Figure 17b clearly shows that, as predicted by the theory and shown on experimental data, elastography can reach the highest levels of CNRe (on the order of 40 dB) at relatively low strains on the order of 0.5 and 1 per cent, where also motion resulting from the compression is the least complex. The discrepancy between theory and experiment at higher strains is most probably due to the unknown elevational decorrelation that has not been accounted for in this theoretical result.

9.4 Applications

The SF can be used to analyse the trade-offs in the strain estimation performance for different ultrasound system parameters, namely with bandwidth and centre frequency [43, 44], algorithms like multicompression [96, 97], temporal stretching [96], multiresolution [44] and extension of the dynamic range in the elastogram [81, 124, 125]. In general, the area under the strain filter computed for a given resolution can be thought of as a very general measure of elastographic quality; the width of the SF describes the quantity of information, while the height describes the quality of that information. Thus improvements in the elastograms may be achieved whenever the width and/or the height of the SF are increased due to any procedure. Two examples of such procedures are described below.

9.4.1 Dynamic range expansion

The strain filter [43] shows the range of strains that can be displayed in the elastogram. For different compressions, however, different tissue elements will experience the strains that fall within the strain filter. The method of variable applied strains [124, 125] is based on the idea of appropriately combining data from different compressions in order to cover the entire strain dynamic range in the tissue. These data are selected according to their value of SNRe. By appropriately scaling these values, depending on the known amounts of applied strain they correspond to, a composite elastogram can be formed containing all the strain values with the highest obtainable SNRe. This corresponds to a shift of the strain filter in logarithmic units by an amount determined by the magnitude of the applied strain. Moreover, due to the slower decorrelation inherent in the strain estimation using the envelope, the use of envelope data helps recover higher strains. By combining these data in the composite elastogram, the strain filter is further extended to the high strain side. Lastly, due to the large amount of data available, averaging can be performed so as to *further* increase the SNRe, i.e. the amplitude of the strain filter. Therefore, a composite strain filter is created that has both a wide elastographic dynamic range (DRe) and a high SNRe (see Fig. 20). This

significant increase in these two essential image quality parameters of elastography is evident by comparison of Figs 18 and 19. They show simulated axial strain elastograms of a finite element phantom containing three circular inclusions that are 10, 20 and 40 dB stiffer than the background (whose elastic modulus is a constant 21 kPa). The single compression elastograms of Fig. 18 are not sufficient to display the high strain dynamic range of the target. However, the combination of dynamic range expansion, envelope information and averaging show a systematic improvement of the image signal-to-noise ratio from Figs 19b to d respectively. The composite elastogram of Fig. 19d depicts the high dynamic range of the target by displaying the difference in strain between the inclusions and by showing the high strain concentration artefact occurring between the top and
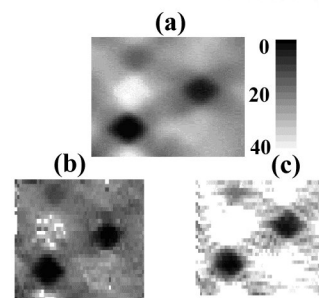

Fig. 18 (a) Ideal axial strain elastogram (from a noiseless finite element simulation) of a three-lesion simulated phantom with a strain dynamic range DRe = 40 dB, (b) elastogram of a single compression at 0.75 per cent applied strain and (c) elastogram of a single compression at 2 per cent applied strain. Note that the full dynamic range of the ideal target cannot be adequately reproduced in either (b) or (c)
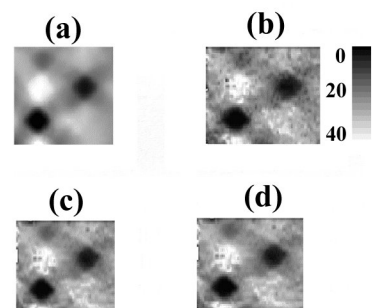

Fig. 19 (a) Ideal strain image for DRe = 40 dB and (b) composite elastogram resulting from the variable applied strain method which extends the dynamic range. (c) Case (b) with added averaging and (d) case (c) with additional envelope processing, further increasing the dynamic range. Note the similarity between (a) and (d) and the vast improvement of all images as compared to those in Figs 18b and c
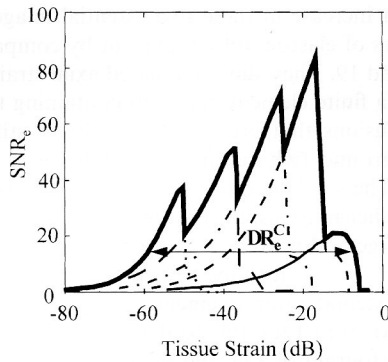
Fig. 20 The composite strain filter (bold curve) is constructed from strain-shifted replicas of the strain filter (broken lines) whose SNRe levels are modulated by the averaging process. The rightmost strain filter is due to signal envelope processing. The combined dynamic range is shown as DRe^C. Actual implementation of this strain filter is shown in Fig. 19

bottom inclusions in the first half of the image. Similar results have been produced experimentally, using a three-layered phantom of 40 dB total stiffness dynamic range, and are shown in Fig. 21. Finally, a similar method has been developed more recently by Lubinski *et al.* [135].
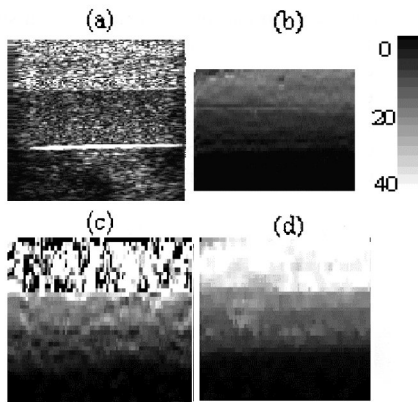

Fig. 21 Experimental results: (a) sonogram of a three-layered phantom with the middle and bottom layers having stiffnesses 20 and 40 dB larger that the top layer respectively (thus, having a total stiffness dynamic range of 40 dB), (b) elastogram obtained with a single compression of 0.5 per cent, (c) elastogram obtained with a single compression of 2 per cent and (d) composite elastogram obtained with the method of variable applied strains using eight compressions at a step of 0.25 per cent. All images are displayed on the same scale as shown. Notice how the composite elastogram allows the total stiffness dynamic range to be visualized and the differences in stiffness between the three layers to be appreciated

9.4.2 Multiresolution elastography

Multiresolution elastography is also described using the SF formulation where the strain estimates with the highest SNRe are obtained by processing the pre- and post-compression waveforms at different window lengths to generate a composite elastogram [44]. A comparison of the elastograms obtained using multiresolution processing as opposed to the traditional method of using a fixed window length is illustrated in Fig. 22. Quantitative values of the SNRe (computed in a small uniform region near the top left corner of the elastogram) and the average resolution (Z_{avg}) in the elastogram are also presented. Z_{avg} is obtained by computing a weighted sum of the window length times the percentage of the strain estimates computed using that window. Note that although the SNRe values for both these elastograms are in the same range, a significant improvement in Z_{avg} is observed in the multiresolution elastogram. For a realistic comparison of the SNRe improvement, the multiresolution elastogram in Fig. 22d should be compared to the fixed resolution elastogram obtained using $Z = 1.7$ mm (Fig. 22c).

The evolution of the SNRe with Z_{avg} for the two techniques is illustrated in Fig. 23. Comparing the techniques at the same Z_{avg} (2.5 mm) indicates a significant improvement in the SNRe (denoted as the increase from A to B). In addition, comparing the elastograms with similar SNRe illustrates the improvement in Z_{avg} (denoted by the improvement from A to C).

The enhancement of the elastographic parameters may also be described in terms of the SF formulation, as illustrated in Fig. 24. In addition to the SNRe enhancement, the dynamic range and sensitivity also improved with multiresolution elastography. Comparing the SFs, it can be seen that DRe = BD is obtained for the elastogram using the fixed window when compared to DRe = BE with multiresolution processing [44].

The properties of the ultrasound imaging system and signal processing algorithms described by the SF can be combined with the elastic contrast properties (CTE) of tissues with simple geometries, enabling prediction of the elastographic contrast-to-noise ratio (CNRe) parameter. The CNRe in elastography is an important quantity that is related to the detectability of a lesion [117].

10 ELASTOGRAPHIC ARTEFACTS

Like any other imaging modality, elastography has various artefacts. The elastographic artefacts can be divided into three primary categories:

1. *Mechancial artefacts.* Strains in the tissue depend not only on the modulus distribution in the tissue but also on boundary conditions, both internal and external. Unlike other artefacts, mechanical artefacts represent true variations in strain; other artefacts generally
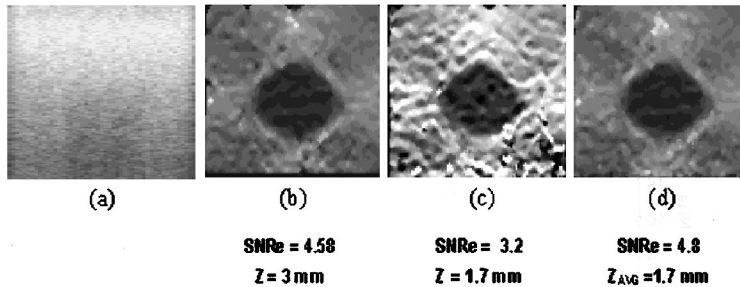
SNRe = 4.58   SNRe = 3.2   SNRe = 4.8
Z = 3 mm   Z = 1.7 mm   Z AVG = 1.7 mm

Fig. 22 Sonogram (a) and elastograms (b–d), with 1 per cent total compression, of a phantom with an inclusion that is three times stiffer than the background. The sonogram was obtained using a 7.5 MHz linear array with a 50 per cent bandwidth. The elastograms in (b) and (c) were obtained using single 3 mm and 1.7 mm windows respectively, while (d) represents the elastogram obtained using multi-resolution elastography [44], with the largest window length used = 3 mm. The image size is 40×40 mm^2
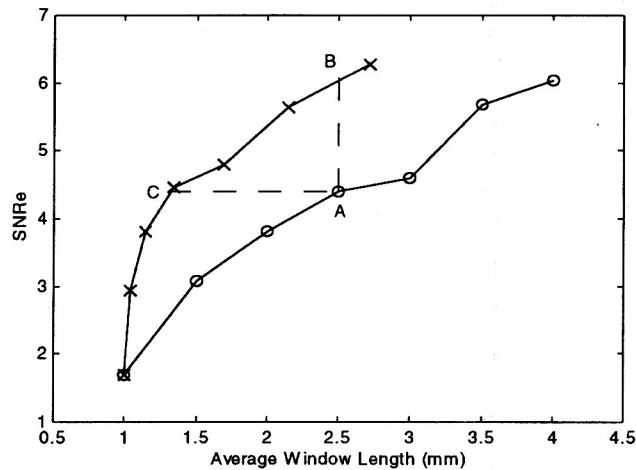

Fig. 23 Comparison of the elastograms obtained using multiresolution ($\times$–$\times$–$\times$) and fixed resolution (O–O–O) elastography. The elastographic SNRe and the average resolution are computed for the elastograms in Fig. 22c (fixed resolution) and Fig. 22d (multiresolution)

hinder an accurate depiction of the strain in the tissue. The mechanical artefacts may sometimes be beneficial, and facilitate diagnosis by highlighting the targets.

2. *Acoustic artefacts.* Estimation of true strain in the tissue is also affected by the ultrasound system.

3. *Signal processing artefacts.* The signal processing algorithms can also introduce significant artefacts into elastograms.

10.1 Mechanical artefacts

Several mechanical artefacts may be present in elastograms [25]. These may include stress concentrations and dilutions due to internal and external boundaries, target hardening artefacts and artefacts due to CTE limitations. In principle, all these could disappear if the perfect modulus reconstruction is made.

10.2 Acoustic artefacts

The ultrasonic scanner used to collect the data has a significant effect on the strain estimation and can introduce various artefacts. Parameters such as large acoustic contrast, changes in the beam, reverberation and phase aberrations can all introduce errors in the elastograms. However, elastography is conventionally a method based on differential measurement, i.e. the pre-compression and post-compression signals generally undergo similar degradations, tending to minimize these artefacts. However, these effects have to date not been thoroughly studied. Some specific acoustic artefacts have been described by Ophir *et al.* [25].

10.3 Signal processing artefacts

Elastography in its present form of development has two major signal processing artefacts, dubbed *zebras* and
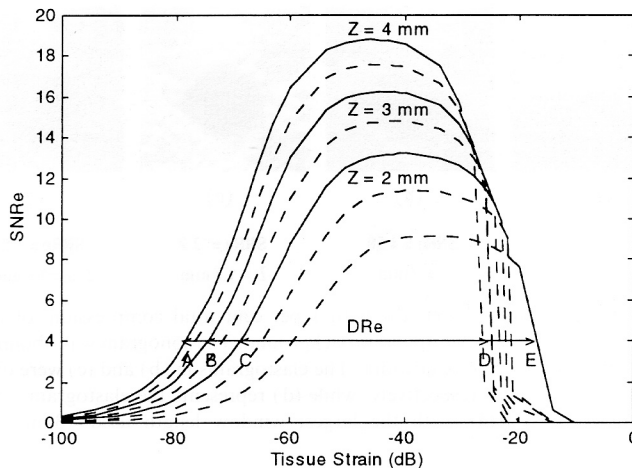
Fig. 24 The multiresolution SFs predicted theoretically for the elastograms shown in Fig. 22. Note the improvement in the sensitivity (minimum strain at the DRe level) with a decrease in elastographic resolution (defined here as the window length)

worms. Elastography is performed on digital signals. Time delay is not generally an integral multiple of the sampling period. Thus, correlation functions can be interpolated to improve the precision of the time delay estimates [126–128]. Elastography commonly uses a parabolic or cosine fit. It is computationally simple, but can introduce a cyclic bias error [52]. If the displacement estimates have a cyclic error, the strain, obtained by taking a gradient of the displacements, will also contain a cyclic error. The authors have determined that any non-linear operation such as the logarithmic amplitude compression greatly enhances this bias error [129]. This bias error manifests itself as horizontal bands of alternate black and white lines on the elastograms. The spatial frequency of this bias increases with increasing strain. Thus this artefact is strain dependent. This particular artefact has been named the 'zebra' artefact [130]. Figure 25a illustrates the appearance of the zebra artefact. This is the elastogram of the tissue-mimicking phantom that has a hard inclusion in a homogeneous background. The elastogram has been processed with log compression of the echo signal and the correlation function has been interpolated with a parabola. The

elastogram has horizontal bands of black and white going through the image. In the region of larger strains, the bands are more closely packed than in the hard inclusion where the strain is lower.

The other signal processing artefact appears when large signal overlaps are used, which produce correlated noise patterns. This artefact also appears as horizontal structures like the zebras. However, there are some important differences. The structures are generally much thinner (vertically) and shorter (horizontally). They do not go through the entire width of the image and are strain independent. This particular artefact has been dubbed 'worms'. An illustration is shown in Fig. 25b.

11 TISSUE IMAGING RESULTS

11.1 *In vitro* elastography

As shown in Fig. 8, for the low-modulus dynamic range, the CTE is close to 0 dB, which means that the strain contrast is nearly equivalent to the Young's modulus contrast. This important observation was recently verified using post-mortem ovine kidneys [11]. For this study a total of 20 kidneys were used. A summary of the results is shown below.

Figure 26 shows matching sonogram, elastogram and a gross pathology photograph of an ROI from a typical ovine kidney, which was embedded in a block of clear gelatin for support during compression. As shown by the sonogram of Fig. 26, the kidney is composed of two different tissue types: the hyperechoic external layer is the renal cortex (RC) and the hypoechoic internal structures (including the renal pyramids and the calices) are known as the renal medulla and sinus (RS). Notice the acoustic shadow just below the renal pelvis. This shadow
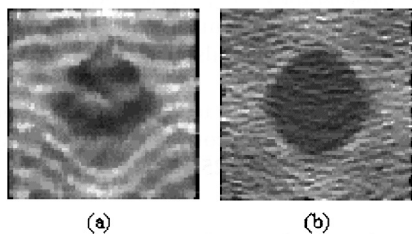

Fig. 25 Inhomogeneous phantom experiment: (a) 'zebra' strain-dependent artefact and (b) 'worm' strain-independent artefact
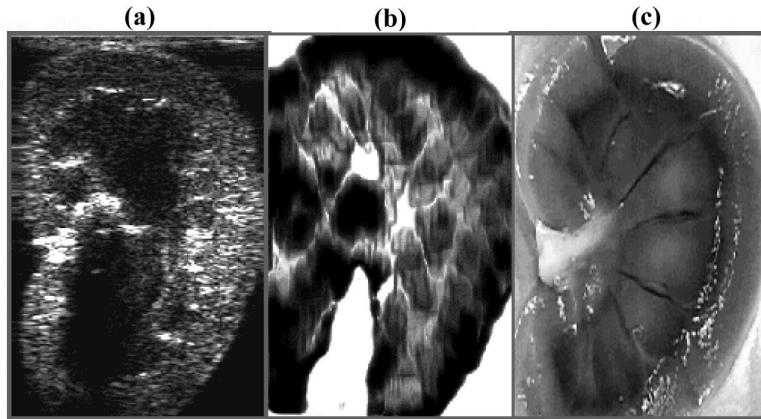
Fig. 26 Longitudinal (a) sonogram, (b) elastogram and (c) pathology photograph of an ovine kidney *in vitro*. In the elastogram, black corresponds to low strain and white to high strain. This elastogram is obtained after a single (0.5 per cent) compression of the gelatin block that contained the kidney. The strains are estimated using a least-squares strain estimator [**75**] applied on displacement data obtained using one-dimensional cross-correlation (1.8 mm window length and 60 per cent overlap). The scan was obtained using the 5 MHz, 40 mm linear array transducer of a Diasonics Spectra II scanner. The elastogram demonstrates structures that are consistent with a stiffer renal cortex and medullary pyramids (of which at least seven are seen), softer columns of Bertin and very soft fatty areas at the base of the columns in the renal sinus. Areas of sonographic echo drop-outs outside the kidney and in the acoustically shadowed areas distal to the renal sinus are intentionally blanked in the elastogram

is due to the high reflectivity of the overlying pelvic tissue. Note the paucity of sonographic detail in the renal medulla and sinus.

From the elastogram of Fig. 26b it can be seen that the strain gradually increases from the RC to the interior of the RS. The strain variation is better illustrated by the plot (Fig. 27a) of the strain across the short axis

of the kidney at the location shown by the arrow (Fig. 26b). This strain variation suggests that the modulus of the kidney tissue gradually decreases from the RC to the RS. This observation was indeed verified using independent measurements of Young's moduli using an Instron testing machine (Fig. 27b). The presence of several stiff, conical areas can also be seen inside the
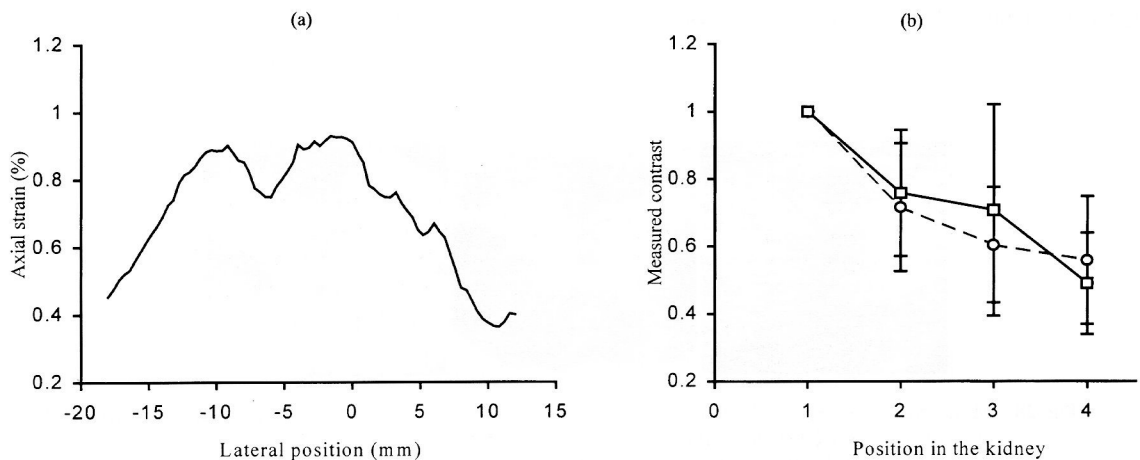
Fig. 27 (a) Strain profile taken from the elastograms of Fig. 26a along the short axis of the kidney at a depth shown by the arrow in Fig. 26b. (b) Modulus contrast measured using the Instron machine (—□—) compared to the strain contrast measured using elastograms (—○—). The Instron and elastographic results were obtained from eight different kidneys. Observe that the modulus contrast variation in the kidney is similar within the error bars to the strain contrast variation. The error bars represent standard deviations

medulla, which are separated by columns. These are consistent with the appearance of the medullary pyramids and the columns of Bertin [131].

As shown by Fig. 27b, the strain contrast is essentially equivalent to the modulus contrast. This experimental result is corroborated theoretically using a model of the contrast transfer efficiency (CTE). Indeed, as shown by Fig. 8, for a modulus dynamic range of less than ± 3 dB, the average efficiency is about -1.46 dB, which also means that the strain contrast is only about 10 per cent less than the equivalent Young's modulus contrast. Therefore, at low contrasts, after controlling the external boundary conditions (compressor size), the elastogram may be interpreted as a quantitative approximation of the inverse of the relative Young's modulus distribution in the tissue. This is an important result that should allow the imaging of actual relative modulus distributions in normal tissues and within various pathological lesions such as tumours, as long as the modulus contrast within these tissues is low ($\leqslant |6$ dB$|$). In such cases, elastic modulus reconstruction may not be necessary.

An example of the visualization of the canine prostate gland is given in Fig. 28. It is evident that the elastographic appearance of the prostate is quite different from that of the sonographic appearance.

11.2 *In vivo* elastography

Because the ease with which compression can be applied to the breast, it is an ideal organ on which to perform elastography. Also, the relative stiffness of breast cancers, as compared to benign fibroadenomas and cysts, makes a method such as elastography which estimates tissue stiffness an attractive tool for distinguishing benign from malignant lesions. For these reasons, virtually all *in vivo* elastography work to date has been performed upon breast lesions [10].

Initially, the procedure was performed on women with suspicious lesions detected mammographically. The woman was examined in the upright position with the breast placed upon the imaging table of a mammography machine. The transducer was attached to a computer-controlled stepper motor, which replaced the compression paddle of the mammography system, and compression was applied downwards on the breast. This had the advantage of providing a stable platform against which to compress the breast. It also allowed elastographic evaluation of non-palpable lesions visible only on mammography, by using a cut-out grid compression paddle with the ultrasound transducer/stepper motor being positioned in the cut-out at the coordinates of the lesion seen on a cranial caudal mammogram.

Between 1993 and 1996, a total of 50 breast lesions were studied just prior to surgical biopsy with this approach using a Diasonics Spectra real-time scanner fitted with a 5 MHz linear array transducer. Radio-frequency data (digitized at 48 MHz) acquired before compression were windowed into 3–6 mm segments and were cross-correlated with similarly windowed data obtained after a 0.3–0.6 mm compression. Up to six elastograms were generated per lesion.

The elastogram is typically displayed side by side with a B-mode sonogram generated from the same RF data. This type of display greatly facilitates identification of lesions on elastography and makes lesion characterization much simpler. Using an elastographic display in which harder tissues are displayed as darker shades of grey, the elastogram often resembles the appearance of an inverse B-mode image. Fatty breast tissue that is dark on the sonogram appears bright (soft) on the elastogram and bright fibroglandular tissue on the sonogram

(a)　　　　(b)　　　　(c)
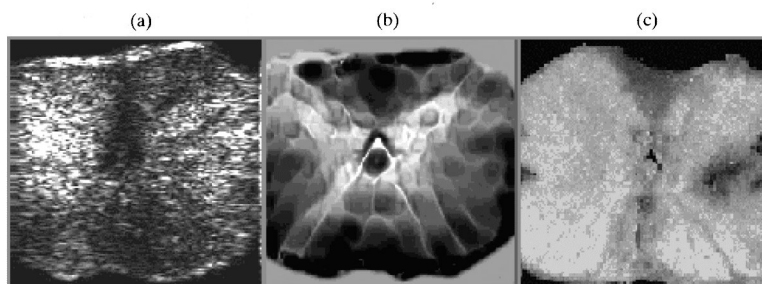
Fig. 28 Matching (a) sonogram, (b) elastogram and (c) gross pathology photograph of an anterior–posterior transverse cross-section of a canine prostate gland *in vitro*. The prostate was obtained immediately after removal and cast in a block of echo-free gelatin. Imaging was done at room temperature with a Diasonics Spectra clinical scanner that had been modified for elastographic imaging, using a 5 MHz, 40 mm array transducer. The field of view is approximately 40×40 mm^2. The elastogram demonstrates anteriorly the isthmus as a low strain area, centrally the verumontanum as a small, dark (hard) circular area just below the lumen of the urethra, which is depicted as an inverted V-shaped soft area. Observe the thin bright lines converging towards the urethra, which are consistent with the prostatic ducts shown on the pathology image

appears darker (stiffer) on the elastogram. Benign fibroadenomas may appear stiffer (darker) than surrounding tissue on elastograms, but often are the same stiffness or softer (brighter) than the surrounding tissue (6 of 15 in the present series). Fibroadenomas generally have smooth regular borders on elastography and their measured size on elastograms was almost always the same or smaller than their diameter on sonography.

Of the 12 cancers that were studied in the initial series, all but one were visible. Most cancers had a stiffer (darker) appearance (Fig. 29) than fibroadenomas but there was considerable overlap in this feature. Cancers often had a mixed appearance with both stiffer and softer areas being present. The transverse diameter of cancers, however, was generally larger on elastograms than on sonograms in all but two cases. This is probably due to the firm desmoplastic reaction surrounding cancers being included as part of the lesion measurement on elastography. Using the combination of lesion stiffness and the difference between the sonographic and elastographic lesion diameters, it was possible to distinguish 8 of 11 fibroadenomas from cancers. This suggests that a significant reduction in biopsies of benign lesions is possible using elastography and sonography together. Also, elastography was found to be useful in the characterization of areas of shadowing on sonograms. Areas of shadowing caused by cancer demonstrated a discrete mass on the elastogram, whereas areas of shadowing caused by poor transducer contact, overlying refraction or mild fibrosis showed no abnormality on the elastogram.

Performing elastography in the upright position led to several problems. The patients were often unable to hold motionless for the time needed to acquire data resulting in useless elastograms. A much more severe problem was the fact that only about 40 per cent of the breast masses were too far away from the chest wall for the ultrasound transducer to access the lesion. In the others, the bulkiness of the transducer and surrounding pressure plate (when held in the vertical position) prevented the ultrasound beam from reaching the lesion. Because of this problem, the next step was to try performing elastography in the supine or oblique supine position, as is done for normal breast sonography. In this situation, the transducer cannot press the breast tissue against a flat surface and the chest wall itself must serve as the base. Since the chest wall has an undulating surface composed of ribs and muscle layers, there was potential for artefacts to be created in the elastogram. The present studies so far have shown this not to be a problem. The supine positioning allows access to all breast lesions and opens the door for a clinically useful elastography instrument.

Noise in elastograms was a significant problem in the first clinical study. This noise was suppressed using five-point median filtration on the final images which reduced the noise but decreased the spatial resolution of the images. To further reduce the noise, the authors have begun to acquire data using multiple compressions. Between three and six compressions are used and the strain data from all pairs of images in the data set are used to generate the final elastogram. An example of a cancer using four compressions is shown in Fig. 30. Further enhancements such as signal stretching should further reduce the noise and allow images to be generated with less noise and higher spatial resolution.

12 SUMMARY AND CONCLUSIONS

The early hypothesis underlying the efforts to measure and image the elastic modulus of tissues has been that

(a)   (b)

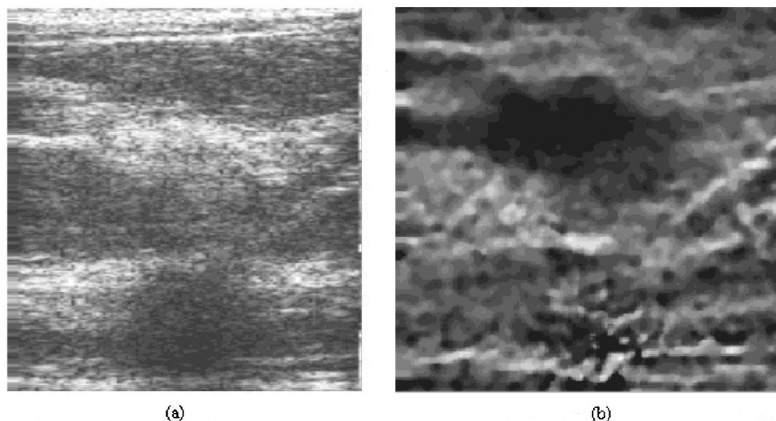**Fig. 29** (a) Sonogram and (b) elastogram of an invasive ductal carcinoma *in vivo* at 5 MHz. Note the irregular mass seen on the elastogram where only an echogenic band and shadow are seen on the sonogram. The lesion is clearly visible as a dark (hard) area on the elastogram, and elastographic structures are visible in the distal sonographic shadows. The elastographic scan size is approximately $40 \times 40 \text{ mm}^2$
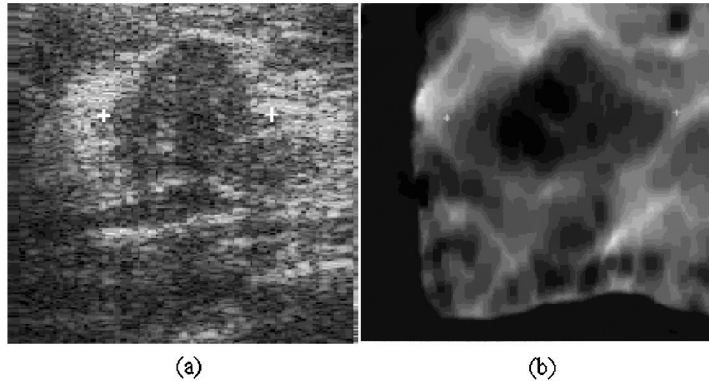
Fig. 30 (a) Sonogram and (b) elastogram (average of four compressions) of invasive ductal carcinoma *in vivo* (noisy areas on the left side and at the bottom of the elastogram have been blacked out). Note the larger size of the lesion in the transverse dimension on the elastogram (crosses). The darkest (hardest) regions of the tumour correspond to the bright foci on the sonogram, which represent microcalcifications. The image size is approximately 40×40 mm^2

soft tissue modulus contrast exists, especially between normal and abnormal tissues. Indeed, it has been shown recently that two important and rather arbitrary tissue contrast domains exist. The first is the existence of a large (> 20 dB) modulus contrast between normal and some pathological tissues (at least in the breast) [50] and the second is the existence of low (< 6 dB) to moderate (< 20 dB) modulus contrast among various normal tissues in the kidney and breast [11, 50]. It has also been shown that procedures such as tissue ablation have a profound effect on tissue elastic moduli [110]. As shown in this article, these observations, together with some initial clinical observations showing the ability of elastography to detect and characterize sonographically occult breast cancers [10], are providing the catalyst for continuing the vigorous development and application of elastographic methods to medical imaging problems.

The estimation and imaging of tissue strains is by definition a three-dimensional problem. When the tissue is compressed, the near incompressibility of most soft tissues means that strain tensor components are generated in all directions simultaneously. Until recently, workers in the field had assumed that single-view ultrasonic methods could not be used for precision lateral displacement and strain estimates [58, 59, 132]. As a result, they are essentially limited to displacement and strain estimations in the axial direction only. Lubinski *et al.* [59] suggested using the precision axial displacements to compute the lateral displacements under a set of assumptions about boundary conditions and incompressibility of the tissue. Konofagou and Ophir [42] have demonstrated that it is in fact possible to make precision estimations of lateral displacements and produce images of lateral strain and Poisson's ratio distributions in tissues, if proper overlap between adjacent ultrasonic beams is maintained. With 1.5-dimensional arrays, or by using a one-dimensional array and measuring the residual eleva-

tional decorrelation after correcting for the other two components, it should be possible to precisely estimate all three longitudinal components of the strain tensor in tissues using clinical array scanners. Poisson elastograms may be important in the imaging of poroelastic, oedematous and other tissues.

Given the existence of significant modulus contrast in many normal and abnormal tissues and the ability to estimate some of the components of the strain tensor, the noise performance of these estimations becomes the important parameter that dictates the achievable image quality with which tissue elastograms can be made. The strain filter framework [43] has been developed to describe the trade-offs among all the technical parameters of the ultrasound instrumentation in terms of their influence on the elastographic image parameters. Using this formalism, it has been demonstrated [43] that axial elastograms with a high SNR, wide strain dynamic range [124, 125] and good strain sensitivity can be achieved at millimetre resolutions. These can be further improved by correcting for lateral displacements [42, 60, 61]. Given, further, that axial or lateral elastograms display the distributions of the respective strains and not of the moduli, a contrast transfer efficiency (CTE) metric has been defined and calculated [45, 46], which adds a description based on elasticity theory of the efficiency with which actual modulus contrast is converted to elastographic strain contrast under known conditions. It has been shown [11] that for low-contrast situations, such as in the normal ovine kidney, the strain image is a reasonable representation of the actual modulus image. For high-contrast situations, inverse problem treatment may be necessary in order to minimize artefacts, as long as there is reasonable knowledge of the boundary conditions. It has also been shown that elastography holds promise in the evaluation of breast masses *in vivo* [10]. Based on the progress described in this article, it is accu-

rate to say that at this point the fundamental aspects of elastographic imaging are reasonably well understood and can be theoretically predicted and practically analysed.

Many interesting challenges remain in the development of this new field. In principle, it should be possible to generate elastograms in real-time, perhaps by reducing the cross-correlation computations to 1-bit hardware operations, which have been shown to be effective [25], or by using fast digital signal processing (DSP) chips. The ultimate limitation on speed is the speed of sound and the speed of propagation of the elastic wave in tissue. The current need for a transducer-holding apparatus is another major limitation. This could be overcome by estimating the unpredictable coarse and fine lateral and elevational displacements [42, 61] encountered in hand-held elastography [72] and correcting the axial elastogram appropriately so that quality images can be generated. This approach is powerful in that it is able to remove severe decorrelation noise that is introduced when the local strain filter *at any point in the image* enters the Barankin bound due to excessive and/or undesired motion [99]. Another solution may involve the use of incoherent strain estimators that are less sensitive to jitter and other undesired motions. A 'stressmeter' in the form of an elastic layer attached to the transducer or the target [24] may be used in conjunction with a hand-held device to allow automatic non-stationary image calibration for uneven compressions. The optimal elastographic protocols that are to be followed when imaging certain tissues are as yet unknown. These include the amount of pre-compression, the applied imaging compression, the number of sonographic frames and the (adaptive) algorithm(s) to be used for image optimization, and the relationship of these protocols to the specific elastic properties (such as contrast and non-linear stress–strain behaviour) of most tissues. While elastographic artefacts are fairly well understood [25], their possibly ambiguous role as detractors or facilitators of lesion detection and/or diagnosis remains unknown. The role of the inverse problem treatment of elastograms [56, 57, 108] and the related definition of tissue moduli at different scales and under variable boundary conditions remains obscure. In principle, these methods could be valuable for reduction of artefacts and for quantitation of elastograms as shown, but major fundamental issues relating to their applicability under various known or unknown boundary conditions must first be resolved. Related techniques, such as high-frequency, high-resolution methods [34, 35] applied intravascularly, may also develop as useful adjuncts to the current sonographic methods. Another important area that could greatly benefit from the incorporation of elastographic techniques is the area of thermal or cryogenic tissue ablation monitoring. It is known that standard sonographic techniques are not well suited for monitoring such procedures due to low contrast. The authors have

recently shown that elastography offers high precision in monitoring laser and high-intensity focused ultrasound (HIFU) applications [110, 133]. The area of elastographic phantom development is another important area that will require attention, since these must be used to objectively test all new developments. Parker *et al.* [48], Hall *et al.* [134] and DeKorte *et al.* [34] have described promising methods for independently manipulating the sonographic and elastographic properties of gelatins to achieve a reasonable range of elastic moduli.

In conclusion, the authors believe that while elastography has progressed rapidly in the past several years, much progress has yet to be made in order for it to become a viable clinical and investigational tool. Even at this early stage, however, it is evident that there exists a fortunate set of favourable biological, mechanical and acoustical circumstances that, when combined, are likely to allow the attainment of this goal.

ACKNOWLEDGEMENTS

REFERENCES

1 **Timoshenko, S. P.** and **Goodier, J. N.** *Theory of Elasticity*, 1970, pp. 403–409 (McGraw-Hill, New York).

2 **Cheney, M.** Inverse boundary-value problems. *Am. Scientist*, 1997, **85**, 448–455.

3 **Carton, R. W., Clark, J. W., Barron, A.** and **Dainauskas, J.** Estimation of tissue elasticity of the lung. *J. Appl. Physiol.*, 1964, **19**, 236–242.

4 **Hayes, W. C.** and **Mockros, L. F.** Viscoelastic properties of human articular cartilage. *J. Appl. Physiol.*, 1971, **31**, 562–568.

5 **Krokosky, E. M.** and **Krouskop, T. A.** A stress deformation model of the human aorta. *J. Biomed. Mater. Res.*, 1968, **2**, 503–525.

6 **Krokosky, E. M.** and **Krouskop, T. A.** The determination of the constitutive relationships for a human aorta. *J. Biomed. Mater. Res.*, 1970, **4**, 525–547.

7 **Saada, S.** *Elasticity, Theory and Applications*, 1983 (Pergamon Press, New York).

8 **Fung, Y. C.** *Biomechanical Properties of Living Tissues*, 1981, Ch. 7 (Springer-Verlag, New York).

9 **Anderson, W. A. D.** *Pathology*, 1953 (C. V. Mosby, St Louis, Missouri).

10 **Garra, B. S., Céspedes, E. I., Ophir, J., Spratt, R. S., Zuurbier, R. A., Magnant, C. M.** and **Pennanen, M. F.** Elastography of breast lesions: initial clinical results. *Radiology*, 1997, **202**, 79–86.

11 Kallel, F., Ophir, J., Magee, K. and **Krouskop, T.** Elastographic imaging of low-contrast elastic modulus distributions in tissue. *Ultrasound Med. Biol.*, 1998, **24**, 409–425.

12 Bakke, T. A new mechanical instrument for the measurement of fibro-elasticity with special reference to its use in the assessment of the consistency of the uterine cervix. *Acta Obstet. Gynecol. Scand.*, 1973, **52**, 277–287.

13 Chen, E. J., Novakofski, J., Jenkins, W. K. and **O'Brien Jr, W. D.** Young's modulus measurements of soft tissues with application to elasticity imaging. *IEEE Trans. Ultrason. Ferroelec. Freq. Control*, 1996, **43**, 191–194.

14 D'Angelo, E. Stress–strain relationships during uniform and non-uniform expansion of isolated lungs. *Respir. Physiol.*, 1975, **23**, 87–107.

15 Fukaya, H., Hildebrandt, J. and **Martin, C. J.** Stress–strain relations of tissue sheets undergoing uniform two dimensional stretch. *J. Appl. Physiol.*, 1969, **27**, 758–762.

16 Galey, F. R. Elastic properties of fixed and fresh muscle. *J. Ultrastruct. Res.*, 1969, **26**, 424–441.

17 Gao, L., Parker, K. J., Lerner, R. M. and **Levinson, S. F.** Imaging of the elastic properties of tissue—a review. *Ultrasound Med. Biol.*, 1996, **22**, 959–977.

18 Harley, R., James, D., Miller, A. and **White, J. W.** Phonons and the elastic moduli of collagen and muscle. *Nature*, 1977, **265**, 285–287.

19 Malinauskas, M., Krouskop, T. A. and **Barry, P. A.** Noninvasive measurement of the elastic modulus of tissue in the above-knee amputation stump. *J. Rehab. Res. Dev.*, 1989, **26**, 45–52.

20 Sarvazyan, A. P. Shear acoustic properties of soft biological tissues in medical diagnosis. *J. Acoust. Soc. Am.*, Proceedings of 125th Meeting, 1993, **93**, 2329.

21 Yamada, H. *Strength of Biological Materials*, 1970 (Williams and Wilkins, Baltimore, Maryland).

22 Demiray, H. A note on the elasticity of soft biological tissues. *J. Biomech.*, 1972, **5**, 309–311.

23 Krouskop, T. A., Vinson, F. S., Goode, B. and **Dougherty, D.** A pulsed Doppler ultrasonic system for making noninvasive measurement of the mechanical properties of soft tissue. *J. Rehab. Res. Dev.*, 1987, **24**, 1–8.

24 Ophir, J., Céspedes, E. I., Ponnekanti, H., Yazdi, Y. and **Li, X.** Elastography: a quantitative method for imaging the elasticity of biological tissues. *Ultrasonic Imaging*, 1991, **13**, 111–134.

25 Ophir, J., Céspedes, I., Garra, B., Ponnekanti, H., Huang, Y. and **Maklad, N.** Elastography: ultrasonic imaging of tissue strain and elastic modulus *in vivo*. *Eur. J. Ultrasound*, 1996, **3**, 49–70.

26 Ophir, J., Kallel, F., Varghese, T., Bertrand, M., Céspedes, I. and **Ponnekanti, H.** Elastography: a systems approach. In *The International Journal of Imaging Systems and Technology*, 1997, Vol. 8, pp. 89–103 (John Wiley, New York).

27 Céspedes, I., Ophir, J., Ponnekanti, H. and **Maklad, N.** Elastography: elasticity imaging using ultrasound with application to muscle and breast *in vivo*. *Ultrasonic Imaging*, 1993, **15**, 73–88.

28 O'Donnell, M., Skovoroda, A. R., Shapo, B. M. and **Emelianov, S. Y.** Internal displacement and strain imaging using ultrasonic speckle tracking. *IEEE Trans. Ultrason. Ferroelec. Freq. Control*, 1994, **41**, 314–325.

29 O'Donnell, M., Skovoroda, A. R. and **Shapo, B. M.** Measurement of arterial wall motion using Fourier based speckle tracking algorithms. In Proceedings of IEEE Ultrasound Symposium, 1991, pp. 1101–1104.

30 Lerner, R. M. and **Parker, K. J.** Sono-elasticity in ultrasonic tissue characterization and echographic imaging. In Proceedings of 7th European Community Workshop (Ed. J. M. Thijssen), Nijmegen, The Netherlands, 1987.

31 Lerner, R. M., Huang, S. R. and **Parker, K. J.** 'Sonoelasticity' images derived from ultrasound signals in mechanically vibrated tissues. *Ultrasound Med. Biol.*, 1990, **16**, 231–239.

32 Yamakoshi, Y., Sato, J. and **Sato, T.** Ultrasonic imaging of internal vibration of soft tissue under forced vibration. *IEEE Trans. Ultrason. Ferroelec. Freq. Control*, 1990, **37**, 45–53.

33 Alam, S. K., Richards, D. W. and **Parker, K. J.** Detection of intraocular pressure change in the eye using sonoelastic Doppler ultrasound. *Ultrasound Med. Biol.*, 1994, **20**, 751–758.

34 DeKorte, C. L., Céspedes, E. I., van der Steen, A. F. W. and **Lancee, C. T.** Intravascular elasticity imaging using ultrasound: feasibility studies in phantoms. *Ultrasound Med. Biol.*, 1997, **23**, 735–746.

35 Ryan, L. K. and **Foster, F. S.** Ultrasonic measurement of differential displacement and strain in a vascular model. *Ultrasonic Imaging*, 1997, **19**, 19–38.

36 Soualmi, L. and **Bertrand, M.** Endovascular elastography: forward problem (Abstract). In 21st International Symposium on *Ultrasonic Imaging and Tissue Characterization*, Washington, DC, 3–5 June 1996.

37 Gao, L., Parker, K. J., Alam, S. K. and **Lerner, R. M.** Sonoelasticity imaging: theory and experimental verification. *J. Acoust. Soc. Am.*, 1995, **97**, 3875–3886.

38 Rubens, D. J., Hadley, M. A., Alam, S. K., Gao, L., Mayer, R. D. and **Parker, K. J.** Sonoelasticity imaging of prostate cancer: *in vitro* results. *Radiology*, 1995, **195**, 379–383.

39 Plewes, D. B., Betty, I., Urchuk, S. N. and **Soutar, I.** Visualizing tissue compliance with MR imaging. *JMRI*, 1995, **5**, 733–738.

40 Fowlkes, J. B., Emelianov, S. Y., Pipe, J. G., Skovoroda, A. R., Carson, P. L., Adler, R. S. and **Sarvazyan, A. P.** Magnetic resonance imaging techniques for detection of elasticity variation. *Med. Phys.*, 1995, **22**, 1771–1778.

41 Muthupillai, R., Lomas, D. J., Rossman, P. J., Greenleaf, J. F., Manduca, A. and **Ehman, R. L.** Magnetic resonance elastography by direct visualization of propagating acoustic strain waves. *Science*, 1995, **269**, 1854–1857.

42 Konofagou, E. E. and **Ophir, J.** A new elastographic method for estimation and imaging of lateral displacements, lateral strains, corrected axial strains and Poisson's ratios in tissues. *Ultrasound Med. Biol.*, 1998, **24**, 1183–1199.

43 Varghese, T. and **Ophir, J.** A theoretical framework for performance characterization of elastography: the strain filter. *IEEE Trans. Ultrason. Ferroelec. Freq. Control*, 1997, **44**, 164–172.

44 Varghese, T., Bilgen, M. and **Ophir, J.** Multiresolution imaging in elastography. *IEEE Trans. Ultrason. Ferroelec. Freq. Control*, 1998, **45**, 65–75.

45 Ponnekanti, H., Ophir, J., Huang, Y. and **Céspedes, I.** Fundamental mechanical limitations on the visualization

of elasticity contrast in elastography. *Ultrasound Med. Biol.*, 1995, **21**, 533–543.

46 **Kallel, F., Bertrand, M.** and **Ophir, J.** Fundamental limitations on the contrast-transfer efficiency in elastography: an analytic study. *Ultrasound Med. Biol.*, 1996, **22**, 463–470.

47 **Sarvazyan, A. P., Skovoroda, A.** and **Vucelic, D.** Utilization of surface acoustic waves and shear acoustic properties for imaging and tissue characterization (Abstract), 1991.

48 **Parker, K. J., Huang, S. R., Musulin, R. A.** and **Lerner, R. M.** Tissue response to mechanical vibrations for sono-elasticity imaging. *Ultrasound Med. Biol.*, 1990, **16**, 241–246.

49 **Walz, M., Teubner, J.** and **Georgi, M.** Elasticity of benign and malignant breast lesions: imaging, application and results in clinical and general practice. In Eighth International Congress on *The Ultrasonic Examination of the Breast*, Heidelberg, Germany, 1993, p. 56.

50 **Krouskop, T. A., Wheeler, T. M., Kallel, F.** and **Hall, T.** The elastic moduli of breast and prostate tissues under compression. *Ultrasonic Imaging*, 1998, **20**, 151–159.

51 **Ophir, J.** and **Yazdi, Y.** US Pat. 5,107,837, issued April 1992.

52 **Céspedes, E. I.** Elastography: imaging of biological tissue elasticity. PhD dissertation, University of Houston, 1993.

53 **Mridha, M.** and **Ödman, S.** Noninvasive method for assessment of subcutaneous edema. *Med. Biol. Engng and Computing*, 1986, **24**, 393–398.

54 **Foster, G. C., Embree, M. P.** and **O'Brien, W. D.** Flow velocity profile via time-domain correlation: error analysis and computer simulation. *IEEE Trans. Ultrason. Ferroelec. Freq. Control*, 1990, **37**, 164–174.

55 **Wilson, L. S.** and **Robinson, D. E.** Ultrasonic measurement of small displacements and deformations of tissue. *Ultrasonic Imaging*, 1982, **4**, 71–82.

56 **Sumi, C., Suzuki, A.** and **Nakayama, K.** Estimation of shear modulus distribution in soft tissue from strain distribution. *IEEE Trans. Biomed. Engng*, 1995, **42**, 193–202.

57 **Skovoroda, A. R., Emelianov, S. Y.** and **O'Donnell, M.** Tissue elasticity reconstruction based on ultrasonic displacement and strain images. *IEEE Trans. Ultrason. Ferroelec. Freq. Control*, 1995, **42**, 747–765.

58 **Kallel, F.** Properties elastiques des tissus mous a partir de l'analyse des changements spatio-temporels dans les signaux ultrasonores. PhD dissertation, Ecole Polytechnique, University of Montreal, Quebec, Canada, 1995.

59 **Lubinski, A. M., Emelianov, S. Y., Raghavan, K. R., Yagle, A. E., Skovoroda, A. R.** and **O'Donnell, M.** Lateral displacement estimation using tissue incompressibility. *IEEE Trans. Ultrason. Ferroelec. Freq. Control*, 1996, **43**, 247–256.

60 **Chaturvedi, P., Insana, M.** and **Hall, T.** 2D companding for noise reduction in strain imaging. *IEEE Trans. Ultrason. Ferroelec. Freq. Control*, 1998, **45**, 179–191.

61 **Chaturvedi, P., Insana, M.** and **Hall, T.** Testing the limitations of 2D companding strain imaging using phantoms. *IEEE Trans. Ultrason. Ferroelec. Freq. Control*, 1998, **45**, 1022–1031.

62 **Alam, S. K.** and **Ophir, J.** Reduction of signal decorrelation from mechanical compression of tissues by temporal stretching: applications to elastography. *Ultrasound Med. Biol.*, 1997, **23**, 95–105.

63 **Céspedes, I.** and **Ophir, J.** Reduction of image noise in elastography. *Ultrasonic Imaging*, 1993, **15**, 89–102.

64 **Varghese, T.** and **Ophir, J.** Enhancement of echo-signal correlation in elastography using temporal stretching. *IEEE Trans. Ultrason. Ferroelec. Freq. Control*, 1997, **44**, 173–180.

65 **Alam, S. K., Ophir, J., Céspedes, I.** and **Varghese, T.** A deconvolution filter for improvement of time-delay estimation in elastography. *IEEE Trans. Ultrason. Ferroelec. Freq. Control*, 1998, **45**, 1565–1572.

66 **Alam, S. K., Ophir, J.** and **Konofagou, E. E.** An adaptive strain estimator for elastography. *IEEE Trans. Ultrason. Ferroelec. Freq. Control*, 1998, **45**, 461–472.

67 **Dickinson, R. J.** Ultrasonic echo analysis in the investigation of soft tissue motion. PhD dissertation, University of London, 1980.

68 **Dickinson, R. J.** and **Hill, C. R.** Measurement of soft tissue motion using correlation between A-scans. *Ultrasound Med. Biol.*, 1982, **8**, 263–271.

69 **Tristam, M., Barbosa, D. C., Cosgrove, D. O., Nassiri, D. K., Bamber, J. C.** and **Hill, C. R.** Ultrasonic study of *in vivo* kinetic characteristics of human tissues. *Ultrasound Med. Biol.*, 1986, **12**, 927–937.

70 **Tristam, M., Barbosa, D. C., Cosgrove, D. O., Bamber, J. C.** and **Hill, C. R.** Application of Fourier analysis to clinical study of patterns of tissue movement. *Ultrasound Med. Biol.*, 1988, **14**, 695–707.

71 **Akiyama, I.** Movement analysis of biological tissues by moving image processing. In Japanese Society of Ultrasound in Medicine Proceedings, 1988, pp. 283–284.

72 **Bamber, C. J.** and **Bush, L. N.** Freehand elasticity imaging using speckle decorrelation rate. In IEEE Symposium on *Acoustical Imaging* (Eds P. Tortoli and L. Masotti), Florence, Italy, 1996, Vol. 22, pp. 285–292.

73 **Varghese, T.** and **Ophir, J.** Estimating tissue strain from signal decorrelation using the correlation coefficient. *Ultrasound Med. Biol.*, 1996, **22**, 1249–1254.

74 **Alam, S. K.** and **Ophir, J.** On the use of envelope and RF signal decorrelation as tissue strain estimators. *Ultrasound Med. Biol.*, 1997, **23**, 1427–1433.

75 **Kallel, F.** and **Ophir, J.** A least squares estimator for elastography. *Ultrasonic Imaging*, 1997, **19**, 195–208.

76 **Alam, S. K.** and **Parker, K. J.** The butterfly search technique for estimation of blood velocity. *Ultrasound Med. Biol.*, 1995, **21**, 657–670.

77 **Alam, S. K.** and **Parker, K. J.** Reduction of computation complexity in the butterfly search technique. *IEEE Trans. Biomed. Engng*, 1996, **43**, 723–733.

78 **Alam, S. K.** The butterfly search blood velocity estimation technique for Doppler ultrasound flow imaging. PhD dissertation, University of Rochester, 1996.

79 **Talhami, H. E., Wilson, L. S.** and **Neale, M. L.** Spectral tissue strain: a new technique for imaging tissue strain using intravascular ultrasound. *Ultrasound Med. Biol.*, 1994, **20**, 759–772.

80 **Bertrand, M., Meunier, M., Doucet, M.** and **Ferland, G.** Ultrasonic biomechanical strain gauge based on speckle tracking. In Proceedings of 1989 IEEE Ultrasonic Symposium, 1989, pp. 859–864.

81 **Varghese, T.** and **Ophir, J.** Characterization of elasto-

graphic noise using the envelope of echo signals. *Ultrasound Med. Biol.*, 1998, **24**, 543–555.

82 **Konofagou, E. E., Varghese, T., Ophir, J.** and **Alam, S. K.** Power spectral strain estimators in elastography. *Ultrasound Med. Biol.*, 1999 (in press).

83 **Varghese, T., Konofagou, E. E.** and **Ophir, J.** Direct and incoherent strain estimation in elastography using spectral cross-correlation, 1998 (in preparation).

84 **Fellingham, L. L.** and **Sommer, P. G.** Ultrasonic characterization of tissue structure in the *in vivo* human liver and spleen. *IEEE Trans. Sonics Ultrason.*, 1984, **31**, 418–428.

85 **Kuc, R., Haghkerder, K.** and **O'Donnell, M.** Presence of cepstral peaks in random reflected ultrasound signal. *Ultrasonic Imaging*, 1986, **8**, 196–212.

86 **Landini, L.** and **Verrazzani, L.** Spectral characterization of tissue microstructure by ultrasound: a stochastic approach. *IEEE Trans. Ultrason. Ferroelec. Freq. Control*, 1990, **37**, 448–456.

87 **Varghese, T.** and **Donohue, K. D.** Characterization of tissue microstructure scatterer distribution with spectral correlation. *Ultrasonic Imaging*, 1993, **15**, 238–254.

88 **Varghese, T.** and **Donohue, K. D.** Mean scatterer spacing estimates with spectral correlation. *J. Acoust. Soc. Am.*, 1994, **96**, 3504–3515.

89 **Varghese, T.** and **Donohue, K. D.** Estimating mean scatterer spacing estimates with the frequency-smoothed spectral autocorrelation function. *IEEE Trans. Ultrason. Ferroelec. Freq. Control*, 1995, **42**, 451–463.

90 **Varghese, T.** Spectral redundancy in tissue characterization. PhD dissertation, University of Kentucky, 1995.

91 **Flax, S. W., Pelc, N. J., Glover, G. H., Gutman, F. D.** and **McLachlan, M.** Spectral characterization and attenuation measurements in ultrasound. *Ultrasonic Imaging*, 1983, **5**, 95–116.

92 **Gerzberg, L.** and **Meindl, J. D.** Power-spectrum centroid detection for Doppler systems applications. *Ultrasonic Imaging*, 1980, **2**, 232–261.

93 **Jensen, J. A.** *Estimation of Blood Velocities Using Ultrasound*, 1996 (Cambridge University Press).

94 **Bahr, R. K., Bucklew, J. A.** and **Flax, S. W.** Optimal center frequency estimation for back-scattered ultrasound pulses. *IEEE Trans. Son. Ultrason.*, 1985, **32**, 809–814.

95 **Kallel, F.** and **Ophir, J.** Three dimensional tissue motion and its effects on image noise in elastography. *IEEE Trans. Ultrason. Ferroelec. Freq. Control*, 1997, **44**, 1286–1296.

96 **Varghese, T., Ophir, J.** and **Céspedes, E. I.** Noise reduction in elastography using temporal stretching with multicompression averaging. *Ultrasound Med. Biol.*, 1996, **22**, 1042–1053.

97 **Varghese, T.** and **Ophir, J.** Performance optimization in elastography: multicompression with temporal stretching. *Ultrasonic Imaging*, 1996, **18**, 193–214.

98 **Konofagou, E. E., Kallel, F.** and **Ophir, J.** Three-dimensional motion estimation in elastography. In 1998 IEEE Symposium on *Ultrasonics, Ferroelectrics and Frequency Control*, Sendai, Japan, 5–8 October 1998.

99 **Kallel, F., Varghese, T., Ophir, J.** and **Bilgen, M.** The nonstationary strain filter in elastography. Part II—lateral and elevational decorrelation. *Ultrasound Med. Biol.*, 1997, **23**, 1357–1369.

100 **Bohs, L. N.** and **Trahey, G. E.** A novel method for angle independent ultrasonic imaging of blood flow and tissue motion. *IEEE Trans. Biomed. Engng*, 1991, **38**, 280–286.

101 **Kallel, F.** and **Bertrand, M.** Tissue elasticity reconstruction using linear perturbation method. *IEEE Trans. Med. Imaging*, 1996, **15**, 299–313.

102 **Ghosh, R. D. N.** *Methods of Inverse Problems in Physics*, 1986 (CRC Press, Boca Raton, Florida).

103 **Bui, H. D.** *Introduction aux Problèmes Inverses en Mécanique des Matériaux*, 1993 (Éditions Eyrolles, Paris).

104 **Gao, Z.** and **Mura, T.** Non-elastic strains in solids: an inverse characterization from measured boundary data. *Int. J. Engng Sci.*, 1992, **30**, 55–68.

105 **Zabras, A., Maniatty, N.** and **Stelson, K.** Finite element analysis of some inverse elasticity problems. *J. Engng Mech.*, 1989, **115**, 1303–1317.

106 **Tikhonov, A.** and **Aresenin, V.** *Solution of Ill-Posed Problems*, 1977 (John Wiley, New York).

107 **Nashed, M. Z.** Operator-theoretic and computational approaches to ill-posed problems with applications to antenna theory. *IEEE Trans. Ant. Prop.*, 1981, **29**, 220–231.

108 **Kallel, F., Bertrand, M., Ophir, J.** and **Céspedes, I.** Advances in tissue elasticity reconstruction using linear perturbation method. In *Acoustical Imaging* (Ed. J. P. Jones), 1996, Vol. 22, pp. 267–277 (Plenum Press, New York).

109 **Rice, J. R.** and **Cleary, M. P.** Some basic stress diffusion solutions for fluid-saturated elastic porous media with compressible constituents. *Rev. Geophysics and Space Physics*, 1976, **14**, 227–241.

110 **Stafford, R. J., Kallel, F., Hazle, J., Cromeens, D., Price, R.** and **Ophir, J.** Elastographic imaging of thermal lesions in soft-tissue: a preliminary study *in vitro*. *Ultrasound Med. Biol.*, 1998, **24**, 1449–1458.

111 **Mak, A. F. T., Lai, V. M.** and **Mow, V. C.** Biphasic indentation of articular cartilage. Part I: theoretical analysis. *J. Biomechanics*, 1987, **20**, 703–714.

112 **Varghese, T.** and **Ophir, J.** A method for experimental characterization of elastographic systems. *Ultrasonic Imaging*, 1999, **21**, 17–30.

113 **Varghese, T.** and **Ophir, J.** The nonstationary strain filter in elastography. Part I: frequency dependent attenuation. *Ultrasound Med. Biol.*, 1997, **23**, 1343–1356.

114 **Quazi, A. H.** An overview of the time delay estimate in active and passive systems for target localization. *IEEE Trans. Acoust. Speech, Sig. Proc.*, 1981, **29**, 527–533.

115 **Knapp, C. H.** and **Carter, G. C.** The generalized correlation method for estimation of time delay. *IEEE Trans. Acoust. Speech, Sig. Proc.*, 1976, **24**, 320–327.

116 **Walker, F. W.** and **Trahey, E. G.** A fundamental limit on delay estimation using partially correlated speckle signals. *IEEE Trans. Ultrason. Ferroelec. Freq. Control*, 1995, **42**, 301–308.

117 **Varghese, T.** and **Ophir, J.** An analysis of the elastographic contrast-to-noise ratio performance. *Ultrasound Med. Biol.*, 1998, **24**, 915–924.

118 **Alam, S. K., Ophir, J.** and **Varghese, T.** Elastographic axial resolution: an experimental study. *IEEE Trans. Ultrason. Ferroelec. Freq. Control*, 1998 (in press).

119 **Bilgen, M.** and **Insana, M. F.** Deformation models and correlation analysis in elastography. *J. Acoust. Soc. Am.*, 1996, **99**, 3212–3224.

120 **Bilgen, M.** and **Insana, M. F.** Error analysis in acoustic elastography: I. Displacement estimation. *J. Acoust. Soc. Am.*, 1997, **101**, 1139–1146.

121 Bilgen, M. and **Insana, M. F.** Error analysis in acoustic elastography: II. Strain estimation and SNR analysis. *J. Acoust. Soc. Am.*, 1997, **101**, 1147–1154.

122 Weinstein, E. and **Weiss, A.** Fundamental limitations in passive time delay estimation—Part I: narrow-band systems. *IEEE Trans. Acoust. Speech, Sig. Proc.*, 1983, **31**, 472–485.

123 Weinstein, E. and **Weiss, A.** Fundamental limitations in passive time-delay estimation—Part II: wide-band systems. *IEEE Trans. Acoust. Speech, Sig. Proc.*, 1984, **31**, 1064–1078.

124 Konofagou, E. E., Ophir, J., Kallel, F. and **Varghese, T.** Elastographic dynamic range expansion using variable applied strains. *Ultrasonic Imaging*, 1997, **19**, 145–166.

125 Konofagou, E. E., Varghese, T. and **Ophir, J.** Variable compressions with RF and baseband processing for dynamic range expansion of elastograms. *J. Med. Ultrason., Jap. Soc. Ultrason. Medicine*, 1997, **24**, 753–760.

126 Boucher, R. E. and **Hassab, J. C.** Analysis of discrete implementation of generalized cross correlator. *IEEE Trans. Acoust. Speech, Sig. Proc.*, 1981, **29**, 609–611.

127 Cusani, R. Fast techniques for time delay estimation. In *Coherence and Time Delay Estimation* (Ed. G. C. Carter), 1993, pp. 78–81 (IEEE Press, New York).

128 Ianniello, J. P. Lower bounds on worst case probability of large error for two channel time delay estimation. *IEEE Trans. Acoust. Speech, Sig. Proc.*, 1985, **33**, 1102–1110.

129 Alam, S. K. and **Ophir, J.** The effect of nonlinear signal transformations on bias errors in elastography. *IEEE Trans. Ultrason. Ferroelec. Freq. Control*, 1998 (under review).

130 Céspedes, E. I., Huang, Y., Ophir, J. and **Spratt, S.** Methods for estimation of subsample time delays of digitized echo signals. *Ultrasonic Imaging*, 1995, **17**, 142–171.

131 Sampaio, F. and **Uflacker, R.** *Renal Anatomy Applied to Urology, Endourology, and Interventional Radiology*, 1993 (Thieme Medical Publishers, New York).

132 Cohn, N. A., Emelianov, S. Y., Lubinski, M. A. and **O'Donnell, M.** An elasticity microscope. Part I: methods. *IEEE Trans. Ultrason. Ferroelec. Freq. Control*, 1997, **44**, 1304–1318.

133 Righetti, R., Kallel, F., Stafford, R. J., Price, R. E., Krouskop, T., Hazle, D. and **Ophir, J.** Elastographic characterization of HIFU-induced lesions in canine livers. *Ultrasound Med. Biol.*, 1999 (in press).

134 Hall, T. J., Bilgen, M., Insana, M. F. and **Krouskop, T. A.** Phantom materials for elastography. *IEEE Trans. Ultrason. Ferroelec. Freq. Control*, 1997, **44**, 1355–1365.

135 Lubinski, M. A., Emelianov, S. V. and **O'Donnell, M.** Adaptive strain estimation using retrospective processing. *IEEE Trans. Ultrason. Ferroelec. Freq. Control*, 1999, **46**, 97–107.